Bergische Universität Wuppertal
Fachbereich C
Mathematik und Naturwissenschaften
Fachgruppe Physik

Analysis of the permittivity data measured at the Pierre Auger Observatory

Bachelor-Thesis

zur Erlangung des akademischen Grades

Bachelor of Science (B.Sc.) im Studiengang Physik

vorgelegt von **Jannis Pawlowsky**

Erstprüfer:	Prof. Dr. Karl-Heinz Kampert
Zweitprüfer:	Prof. Dr. Christian Zeitnitz
Abgabedatum:	25.10.2018

Contents

List of Figures

List of Tables

1 Introduction

The Pierre Auger Observatory is based in Argentinia and is the world's largest experiment by area [1]. The scientific goal is the detection of cosmic rays and their properties such as origin and composition. The observatory consists of different detector types. Beside the detection with photomultipliers, the hybrid detector consists of antennas measuring the electromagnetic radiation emit. The Auger Engineering Radio Array (AERA) currently comprises an array of about 150 antennas to measure this signal [2].
As the cosmic rays arrive from the universe, the emitted radio signals, generated in the atmosphere, propagate from the sky towards the array. However, a non-negligible part of the measured amplitude is caused by signals hitting the antennae after being deflected off the ground [2].
This circumstance calls for further investigation in its effects on the measured signal. The reflection and transmission of electromagnetic waves depend mainly on the medium [3]. The quantity describing this behaviour is the relative permittivity. Aside from the material specific value, it changes with the frequency of the electromagnetic wave and enviromental aspects such as moistness and temperature. As the observatory is exposed to various weather conditions, there are a multitude of factors that can influence the ground's permittivity, its reflection coefficient and eventually the reflected signal. Because of this, it changes its reflection coefficient and influences the signal. Up to now, the reconstruction of the signals were made by assuming a constant value for the relative permittivity.
This thesis discusses exactly this apect. How stable is the permittivity for field conditions and is the constant an acceptable approximation? To answer this question, data from the last three years was analysed, that was acquired using a setup designed in [4] in the scope to measure the permittivity of the soil over extended time periods.
Before the setup will be presented in chapter 3, the basic concepts of cosmic rays and the Pierre Auger Observatory are discussed in chapter 2. Section 4 deals with the measured data, its structure and in particular its quality. This should give an impression of the significance of the analysis detailed in chapter 5. In particular, the dependence of different enviromental influences is shown and how the permittivity develops in time. In the subsequent chapter, the cosmic background is investigated, as well as the effect of the permittivity on the signal. The thesis concludes with the summary.

2 Cosmic rays and their measurement at the Pierre Auger Observatory

In this chapter, the fundamental aspects of cosmic ray physics are discussed. It gives a quick impression, why investigating high energy particle from space is of significance and could be a pathway for new physics. Subsequently, a techniques for measuring cosmic rays are presented, based on examples from the Pierre Auger Observatory.

2.1 Cosmic particle showers

In 1936 Victor Hess was awarded the Nobel Prize for discovering between 1911 and 1913, that the majority of the radiation on earth have its origins in the outer space. He measured the radiation at different altitude, while flying balloons up to 5.3km [5]. The fact that the radiation increased with the height lead him to the conclsuion that the main part of radiation has to propagate from outer space towards the earth. This discovery was the birth of a new branch of physics, namely particle physics. Since then, the types of measurement, the experiments and discoveries changed and developed rapidly.
The cause for cosmic ray showers are high energetic particles [6]. In this case, high energetic means energies up to 10^{20} eV. As they hit the atmosphere, they interact with the nuclei of its atoms. These interactions split the energy of the first particle to numerous more particles of different energy. This process is decribed amongst others by the Heitler model [7]. Here, particle showers can be seperated into electromagnetic and hadronic showers. Bremsstrahlung and pair production dominate the electromagnetic one, while the interaction of particles make up the hadronic shower [6].
After N interactions ($N \in \mathbb{N}$, depending on energy and type of primary particle), the energy of the secondary particles drops below a critical value E_c, where ionization losses dominate the process. At this point, the amount of particles is at its maximum. Measuring this number contains information about the energy and type of the primary particles. The sum of all produced particles make up the cosmic ray flux, as seen in Fig. 1a. This spectrum, measured by the Pierre Auger Observatory, helps us answer questions about energy, composition and rate of high energy cosmic rays. On the other side, there are still existing and also unexplained processes. For example staying focused on this spectrum, an irregularity can be seen at an energy of about 10^{18} eV (this point is the so-called 'ankle') [1]. The origin of this break also gives insight into origin and acceleration of high energetic particles.
Currently, several experiments are dedicated to investigate the multitude features cosmic rays reveal. One of the most famous experiments, and the largest by area, is the Pierre Auger Observatory. The measurements and the detectors are discussed in the following section.

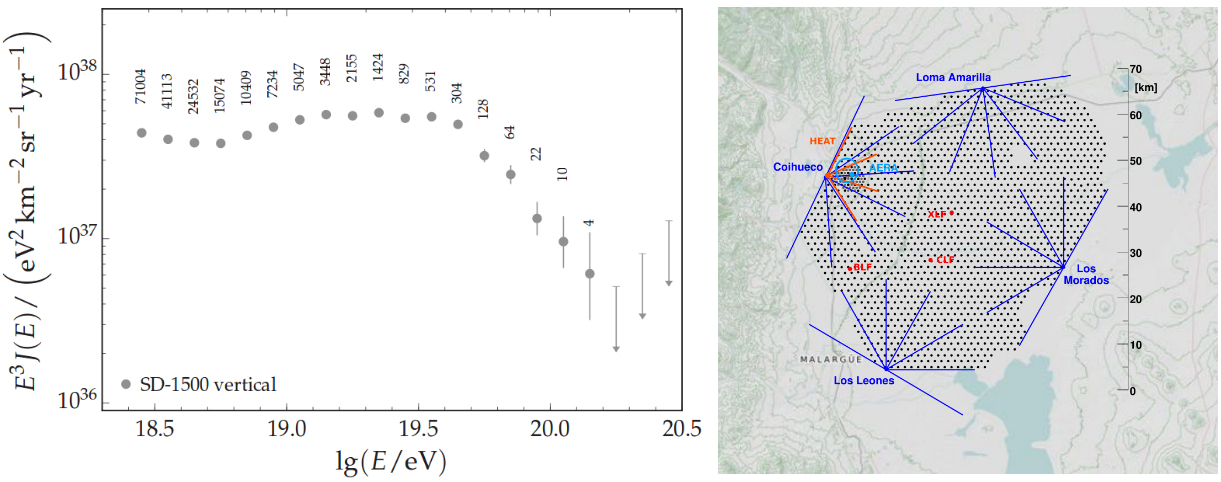

(a) (b)

Figure 1: **(a)** The cosmic ray flux is shown; the numbers indicate the frequency of this energy. **(b)** The figure shows the Pierre Auger Observatory. Each black dot represents a Water Cherenkov detector. The blue and red lines show the viewing area of the flurouscence detectors. The cyan circle marks the field of radio antennas. Picture (a) from [8], picture (b) from [1].

2.2 The Pierre Auger Observatory

The Pierre Auger Observatory is set up in Argentinia near Malargüe and was officially completed in 2008, after eight years of building. Since the amount of measured cosmic rays is dependent on the area, the idea was to extend an area as large as possible. Today this area is about 3000 km^2 large [1], which is similar to the area of Luxembourg. The area is covered by more than 1600 Water Cherenkov detectors (WCD) with a dinstance of 1500 m to neighbouring stations [1]. The other detector types are fluroscence detectors, WCDs and radio antennas (the specific attributes of these parts are discussed in section 2.2.1, 2.2.2 and 2.2.3). In Fig. 1b, the observatory is depicted in its entirety.
Through its large area and long runtime, the observatory recorded a large number amount of air showers. In Fig. 1a the numbers above the data points represent the amount of measurements of each energy bin until 2013. This is a good statistic, but even more important is the ability to analyse it. Energy, type and arrival direction are the most interesting values.
To improve the shower reconstruction, especially the discimination of the myonic and electromagnetic component, the Auger Prime upgrade was initiated. It includes the upgrade of existing detectors as well as the introduction of new detectors [1]. A main point is to add surface scintillators to the WCDs, which are presented in the following chapter.those

2.2.1 Surface detector

The WCDs are 12 m^3 water filled tanks [1], in which the relativistic particles produce Cherenkov light. This is recorded by three photomultipliers for each station. Neighbouring stations measure the cosmic ray showers nearly at the same time. The WCDs measure muons, electrons and photons. For better seperation, the idea is to add a surface scintillator detector (SSD). The detector consists of two plastic scintillators with a surface of about 2 m^2 [1], which are mounted on top of the WCD. In Fig. 2 a WCD with a prototype of a SSD on top can be seen.

Figure 2: The WCD (yellow colour) and the SSD are depicted from the side. Picture from [1].

2.2.2 Flurouscence Detectors

Another way to measure cosmic rays is to observe flurouscence light emitted after interactions in the atmosphere. The light is measured by the five flurouscence detectors (FD). The produced light is emitted isotropically in the atmosphere. Hence, a fraction of the photons travel towards the FD. There, the beam gets bundled by a system of concave mirrors. The light hits a grid of photomultipliers [1]. The detector measures time, amplitude and arrival direction of the beam, which allows for the reconstruction and visualisation of the shower developement in the atmosphere.
The FDs are very sensitive to light, therefore they need certain cirumstances to work properly. The biggest restriction is that they only measure at moonless nights with clear skies. Secondly, the shutter of the detector has to be closed, if it is raining or storming to protect the optical surface. Hence, the duty cicle is limited to about 15% of time. To extend the duty cicle the photomultipliers are operated with lower supply voltage. Tests show that the detector can work at nights with a fraction of the moon still visible.

(a) Picture of the LPDA (b) Picture of the butterfly antenna

Figure 3: The graphics show the both antenna types setup in Argentinia. Pictures from [9].

2.2.3 Radio measurement at AERA

The FDs and WCDs were built at the beginning of the experiment. In contrast to that, another type of measurement has been developed later on, the Auger Engineering Radio Array. AERA first started as a task from the collaboration in 2009, after first radio measurements started September 2006. Since then, it has developed, now being an official part of the observatory. AERA covers 17 km^2 with more than 150 antennas, deployed in different phases [2]. The array started with 24 densely spaced stations in 2011, extended by 100 antennas in 2013 and was finalized by 29 antennas in 2015. Each set of antenna forms a grid and is specialized for specific purpose. The first antennas were mainly used for testing and construction of rather low energetic signals. The second set expanded the measured energy scale and the third one is optimised for horizontal air showers. The purpose is determined by the grid spacing and the antenna type.

The first type is just used in phase one and is the so called logarithmic-periodic dipole antenna, the second type is the butterfly antenna. Figure 3 shows the antennas. Especially the butterfly antennas get a rather large fraction of their signal by reflections from the ground [9]. As AERA made huge progress, the AugerPrime also includes the extension of all stations with radio detection. The fully funded plan includes mounting of the so-called SALLA antennas on top of each SD. Thereby, the informational content should increase and new features of events could be discovered, that are only detectable with antennas. As an example the events can be mentioned, where the footprint of the radio signal was larger than particle footprint. For these horizontal extensive airshowers the information can be substantially increased by the radio measurement.

Since the knowledge about outer influences is indispensable for AERA, the permittivity is also part of discussions and was measured by different setups. One of them is the basis for this thesis. It will be presented in the next chapter.

3 Permittivity and measurement

3.1 Absolute and relative permittivity and electric conductivity

The absolute permittivity ε of a medium is also called distributed capacitance [3]. This name gives an impression of the effect it has. As an electromagnetic wave propagates through a dielectric medium, the permittivity is the degree of permeability of the medium for an electric field $\vec{E}$, as the inner polarization counters the electric waves:

$$\vec{D} = \varepsilon \vec{E},$$

with the electric displacement field $\vec{D}$. Replacing $\varepsilon = \varepsilon_0 \varepsilon_\mathrm{r}$ gives:

$$\vec{D} = \varepsilon_0 \varepsilon_\mathrm{r} \vec{E}. \tag{1}$$

Here, $\varepsilon_0 := \frac{1}{c_0^2 \mu_0} \approx 8.85 \cdot 10^{-12} \frac{\mathrm{F}}{\mathrm{m}}$ [3] is the vacuum permittivity and ε_r is also known as the dimensionsless relative permittivity or dielectric constant. The designation as a constant is misleading, since ε_r is dependent on several parameters.
ε_r is material-dependent, and in most cases greater than 1 (there are special cases like plasma, where ε_r can be less than 1). ε_r marks the factor by which the electric field gets attenuated inside a medium compared to the field in vacuum. In addition, the relative permittivity is related to the reflection and transmission of electromagnetic waves when hitting a medium boundary. Using Maxwell's equations [3] one obtains

$$n = \sqrt{\varepsilon_\mathrm{r} \cdot \mu_r}, \tag{2}$$

where μ_r is the electromagnetic permeability and n the refractive index. Carrying on, the refractive index is related to the reflection and transmission of a medium ([10] for more informations).
At this point, the reason for investigating the relative permittivity is revealed. The relative permittivity is more useful and handy information than the absolute permittivity. Therefore **the relative permittivity will just be called permittivity** from now on for reasons of simplicity. As already mentioned in the previous section, the antennas of AERA are not just sensitive to signals coming from the top, but also from the ground deflected signals. Especially at times, when the permittivity is rather low, a great proportion gets reflected and hit the antennas from below. This raises the question, which parameters, besides the material of the medium, have an effect on the value of the permittivity.

3.2 Polarization of materials

Looking for the dependencies, it should be explained in detail, how polarization of a medium occurs and which effect it has. The easiest way to describe this is imagining the

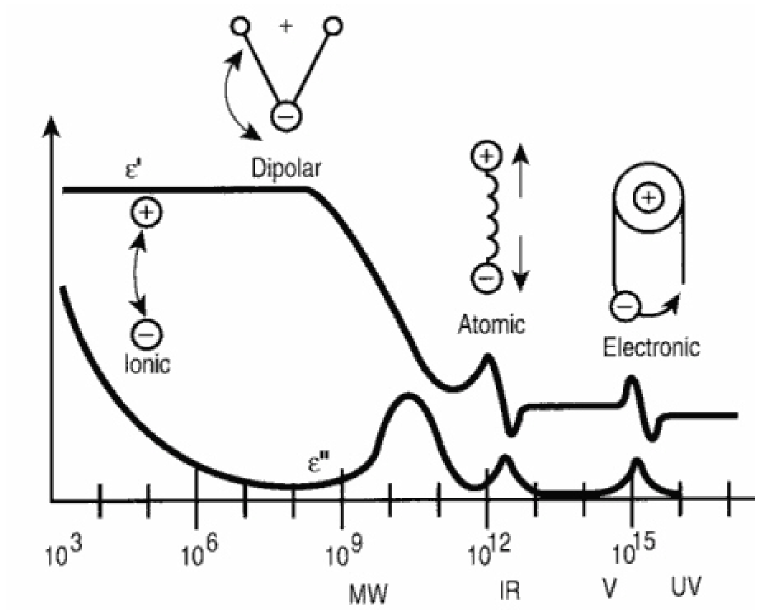

Figure 4: Schematic development of the permittivity (ε') and the heat loss (ε''). Their relative value is depicted by the y-axis, the frequency [Hz] can be seen on the x-axis. The heat loss is often seen as the complex part of the permittivity. Plot from [11].

medium inside of a capacitor. The outer electric field of the capacitor forces a change in the orientation of dipoles (like molecules) through the electromagnetic force. The dipoles form an inner electric field weakening the outer field. The strength of attenuation is determined by the medium and its atomic bonds. For example water can be easily polarized, hence it strongly weakens the outer electric field and has a comparatively high permittivity.

The direct voltage of the capacitor can also be replaced by alternating voltage. The resulting behaviour is shown in Fig. 4. For rather low frequencies ($f < 1$ GHz), the permittivity nearly stays constant as the change of orientation is slow enough. However, the energy loss is high. Due to exchange of ions there is huge heat generation. The loss decreases as the frequency increases and the probability for the effect vanishes. For frequencies greater than 1 GHz, the dipoles can not follow the change of orientation without delay. As a result, the permittivity drops and only peaks again when hitting the resonance frequency of the atoms or electrons.

The relevant frequency band for radio measurement at AERA ranges from 30 to 80 MHz. Therefore, the permittivity measured and analysed should have a rather low frequency dependence.

Another parameter influencing the permittivity and which is correlated to the polarization, is the temperature. The temperature affects the movement of molecules. Crystalline structures like ice hinder the movement and thereby also hinders the orientation of dipoles. Heating the water increases the motion and lets the bonds break more easily. Up to a certain temperature (for water about 40°C), the permittivity rises due to this effect. Further heating leads to greater molecule movements and influences the orientation of

dipoles. The impact is smaller for other materials, nevertheless it should be investigated, due to the large temperature spread in Argentinia (-20°C at some nights and up to 40°C at daytime).
Both parameters affect the permittivity, but the greatest influence still stems from the medium. Table 1 should give an impression of this behaviour. A further discussion about the types of soil at the Pierre Auger Observatory will be made in section 4.4. The debate about the influence of the moisture of the ground (resulting from rain for example) will be a main part of the analysis in this thesis and is presented in chapter 5.

Table 1: Permittivities at room temperature [12]

Material	ε_r	Frequency		Material	ε_r	Frequency
Dry sand	2.5	1 MHz		NaCl	≈ 6	1 kHz - 10GHz
Moist sand	9	1 MHz		Air	≈ 1	1 kHz - 10GHz
Dry soil	3	1 MHz		Silicon	11.7	1 kHz
Most soil	10	1 MHz		Water	80.1	1 kHz

3.3 Measurement of the permittivity

The setup in Argentinia is based on a diploma thesis [4]. The main component is the vector network analyzer (VNA) [13]. The VNA produces a signal of certain frequency, which is then passed on to a probe (see Fig.). At this point, the impedence of the probe can be measured. This gives information about the reflection and transmission of electromagnetic waves and the resulting phase angle of the signals.
These quantities help us determine parameters such as resistance, impedence and phase angle of the impedence. The permittivity can be calculated by these parameters, the exact derivation can be seen in the thesis and will not be repeated here. The result is the formular for calculating the permittivity:

$$\varepsilon_r = \frac{1}{2\pi f C_0}\left(\frac{\tan\theta}{|Z|\sqrt{1+\tan^2\theta}}\right). \tag{3}$$

Here, f is the frequency used by the VNA, $|Z|$ is the measured absolute impedence of the probe and θ its phase angle. C_0 is a reference value for the capacity in air from the used aluminium probe. This was determined to be

$$C_0 = 5.36\text{pF} \pm 0.02\text{pF}.$$

The setup can be cotrolled by a Raspberry Pi. The software [14] as well as the calibration file for the VNA are installed on the computer. The calibration was made for the VNA, which was mounted at the beginning of the measurement in April 2015. After a year, the VNA was changed [15]. As the second VNA is the same model as the first one, the

conclusion was made that a new calibration is not necessary or at least could be made later. It will be seen, this decision turned out to be erroneous. The setup can be seen in Fig. 5, the probe is buried in the soil beside the box. Also seen in this figure is the battery. It is charged by a solar panel for autonomous operation. The whole setup is located at a weather station, the AERAWS.
The resulting quality, before and after the change of the VNA, is discussed in section 4.4. But first, the following chapter presents the amount of required data and why the VNA had to be changed at all.

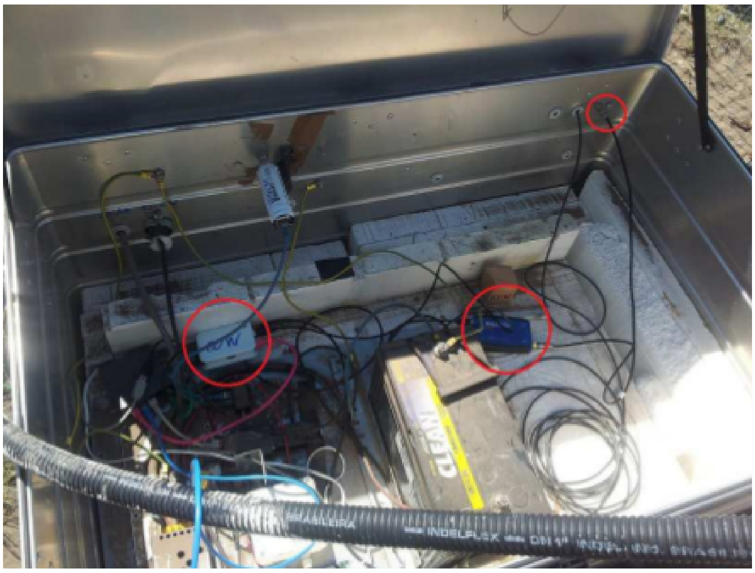

Figure 5: The setup is visible. The circles mark from the left to the right the Rasberry Pi, the VNA and the connection to the probe. Picture from [14].

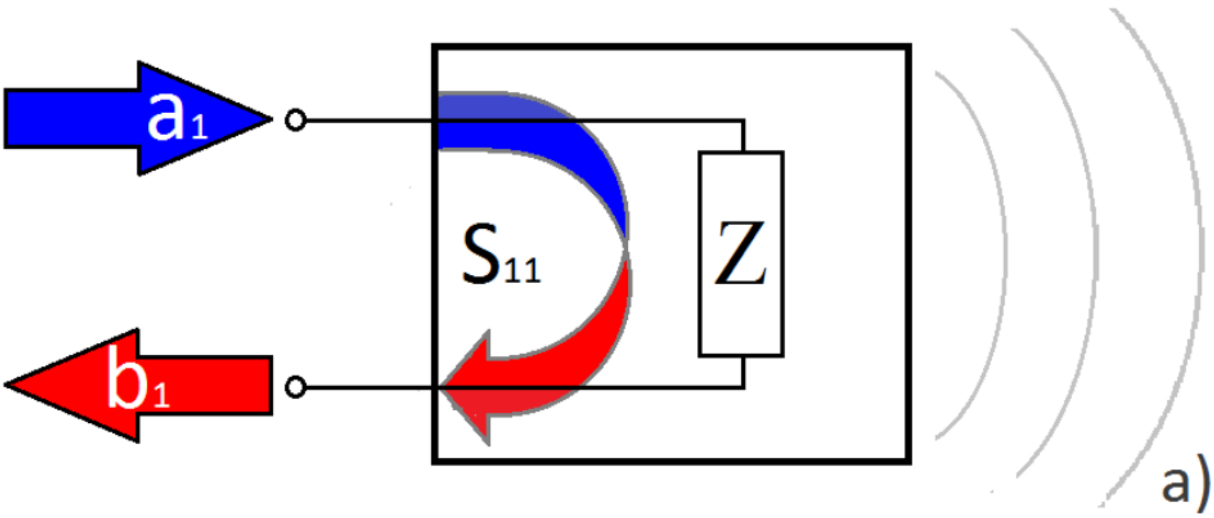

Figure 6: The schematic functionality is depicted; the VNA produces the signal a and measures the transmitted signal. Picture from [14].

4 Investigation of the permittivity data

All plots in this chapter are presented without errorbars. This will be explained in chapter 4.4.

4.1 Structure and amount of the data

The data is saved in CSV-format. Every 15 minutes (the first two months the time gap was one hour) the VNA acquires data for 200 different frequencies. The frequency ranges from 0.1MHz up to 199MHz, therefore the stepsize is about 1MHz. The basic data measured is the complex impedance and the phase angle of the signals. In order to get useful and readable information, the Raspberry Pi calculates return loss, omic resistance, standing wave ratio, capacitive resistance, and the absolute value and phase angle of the impedance.
To get a better overview and reduce unneccesary reading of files, the first step is to write each quantity via script into a table. For each quantity, a table of 33964 data points multiplied by 200 frequencies is produced. One can see, since the beginning of measurement in april 2015 until the end of 2017, there should be about 70000 data points, which means the setup was recording less than half the time. This circumstance can be tracked back to a malfunctioning of the VNA. The first VNA used crashed frequently. When it crashed it has to be restarted again manually. Due to the observatories size, a normal maintenance cycle for stations is about 3 years. Consequently, the VNA could only turned on again if someone knowing this circumstance is already in Argentinia and does an extra tour for this purpose. As a result, we see blank periods between the beginning and end of 2016, when no data was taken. In November 2016 the VNA was replaced by one of the same type. In addition, the Raspberry Pi was replaced by a Banana Pi with internal memory. Since then, the VNA has not crashed as frequently as before. In Fig. 7, the cumulative amount of data acquired as a function of time is depicted. Although the VNA did not work as often as expected, the amount of data seems to be sufficient for a meaningful analysis. There are weeks in which the VNA acquired data continuously. Furthermore, the data is from different months. Judging them just by amount and distribution of data points, an investigation of the time and weather dependence should be possible. As will be seen, the quality of data is the more significant factor and constitutes the greater challenge in the analysis.

4.2 Quality of the data

All dates and frequencies and the respective permittivity are plotted to a heatmap. This is done in Fig. 8.
Even without a clear idea of the expected trend for the permittivity, it is clear that it contains irregularities. The figure will be discussed part after part, marked by the numbers. For this and all follow heatmaps the time scale is sorted, but not steady, periods in which

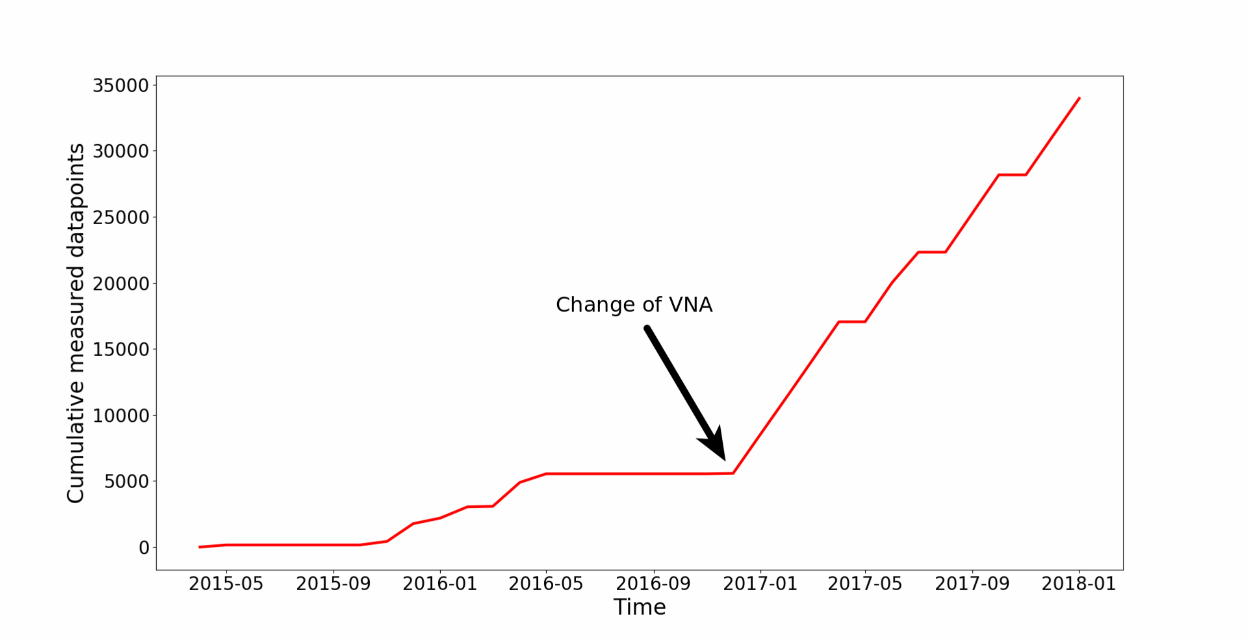

Figure 7: Measured data plotted against the time.

no data was acquired are left out and the colourscale is limited from -3 to +3, as the majority of the values are between those bounds. This way, specific features are more visible. The values outside of this range are shown as -3 or +3, respectively.

For **part I**, the plot demonstates a steady progress until the 4th of December in 2015. Figure 9 shows this part in a finer time scale.

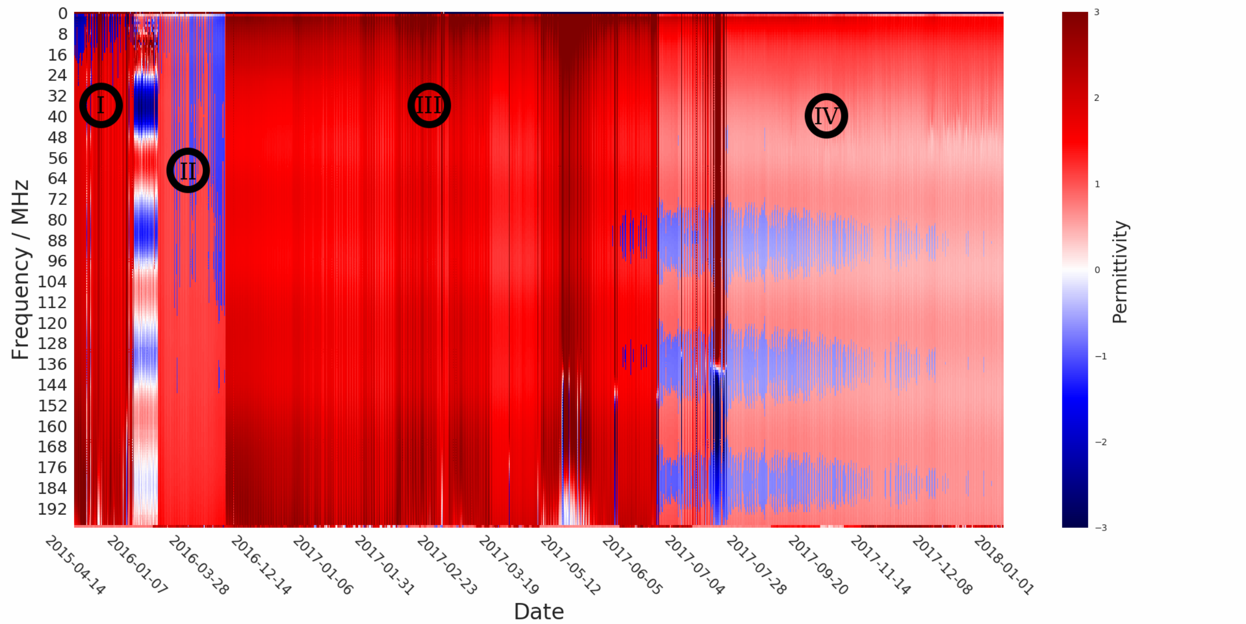

Figure 8: The permittivity as function of the date measured and the respective frequency; the numbers in the plot represent the sections, in which the figure can be separated.

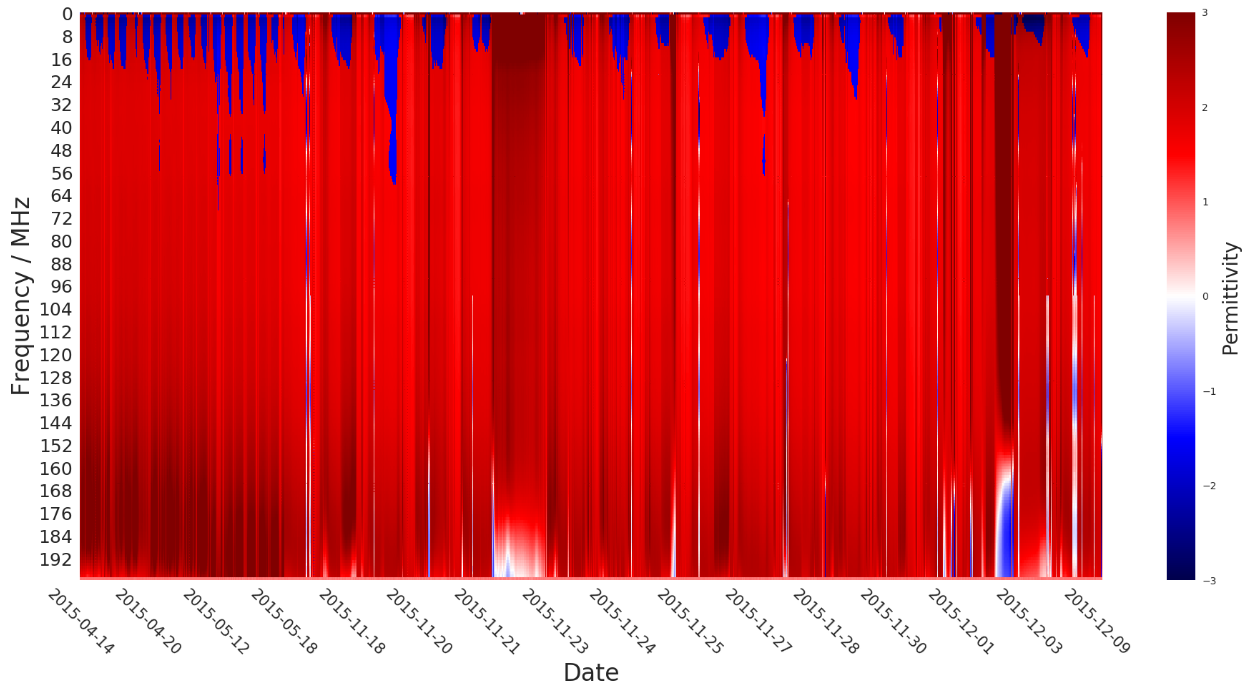

Figure 9: Zoomed part I of the heatmap in Fig. 8.

Almost all values are greater than one. In addition, the development seems continuous. However, there are times when the permittivity has negative values. This appears especially for higher and lower ends of the frequency range. The reason for negative values will be explained in detail in part IV. Nevertheless, the mentioned frequencies are strange the whole time. A possible explanation for this behaviour can be determined from the specifications of the VNA [13]. The frequency range from 1 MHz to 200 MHz is fully measured, the edges of the band might not work right as they do in the middle. Another aspect to mention are the white stripes in the plot. These are single measurements differing from the rest. In Fig. 10, a comparision is made between one of this kind and a regular measurement. The plot shows an oscillating behaviour around zero for the red dots. The blue points indicate a regular measurement. A malfunctioning of the VNA can be assumed, most likely caused by the battery of the VNA. This concept will be explained in detail for part II. Other options like an outer eletrical field influencing the setup have been checked by looking into the respective data of the observatory and have been falsified. It is assumed that it is an internal error. Datasets of this kind will be sorted out later (see section 4.3). Nevertheless, the majority of datapoints appears reasonable.

After the last datapoint of part I, the setup stopped acquiring data. Until the replacement of the VNA, it acquired the data shown in Fig. 11 from **part II**.

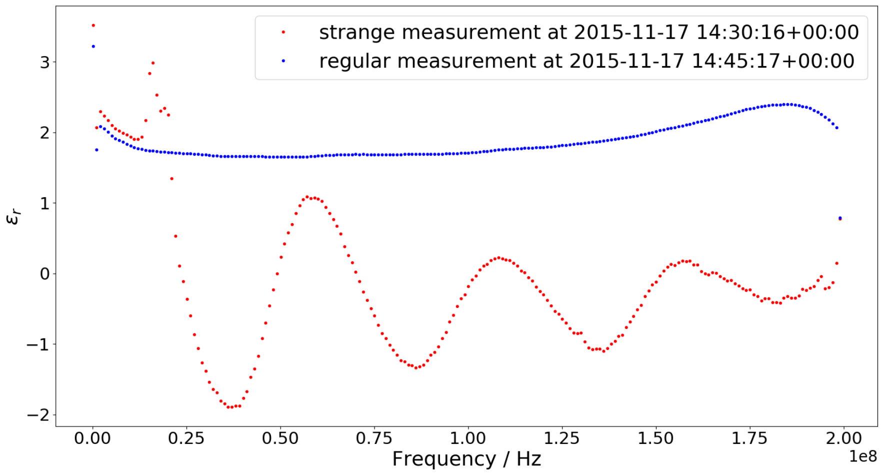

Figure 10: The blue points represent a typical measurement. The red points are similar in the beginning but start an oscillating behaviour after a while.

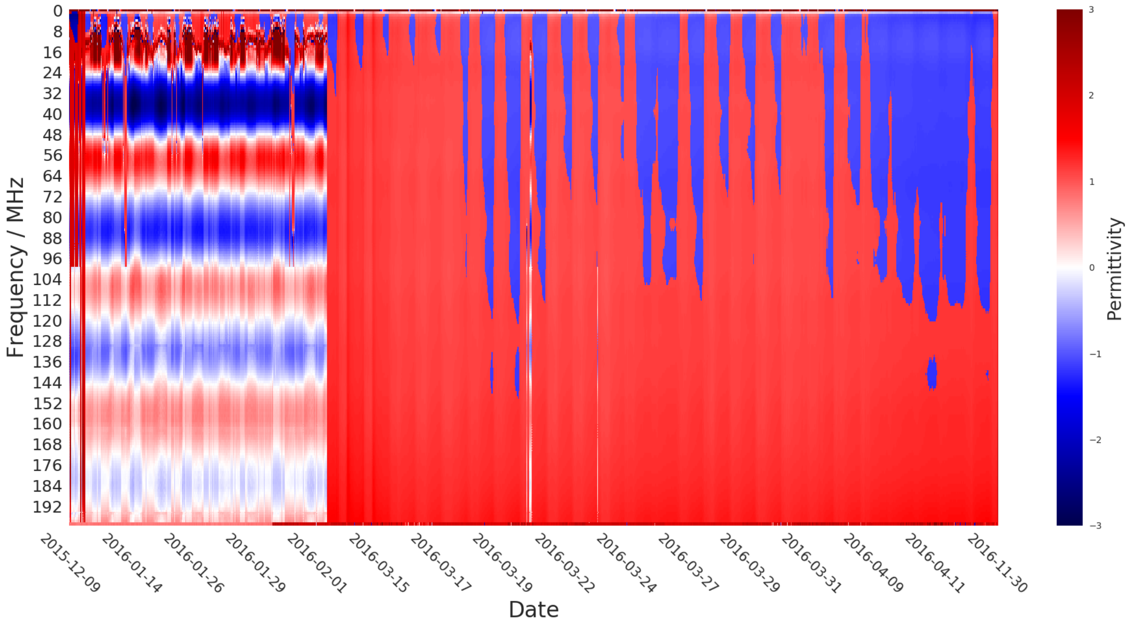

Figure 11: Zoomed part II of the heatmap in Fig. 8.

The recording periods are very sparse and short. The setup is clearly malfunctioning. This could be related to the weather station, to which the setup is located nearby; AERAWS also acquired data just half of the time. As the malfunctioning of AERAWS is caused in this time by insufficient power supply, it would most likely apply for the permittivity setup as well (both work with solar panels). A hint for this can be seen at the beginning of the heatmap. Figure 12 shows one of these datasets. For low frequencies, the development is as expected. Later on, a radical change appears and the permittivity starts oscillating around zero. This could be explained by the following.
The programming code for the software of the VNA could not be provided, nevertheless,

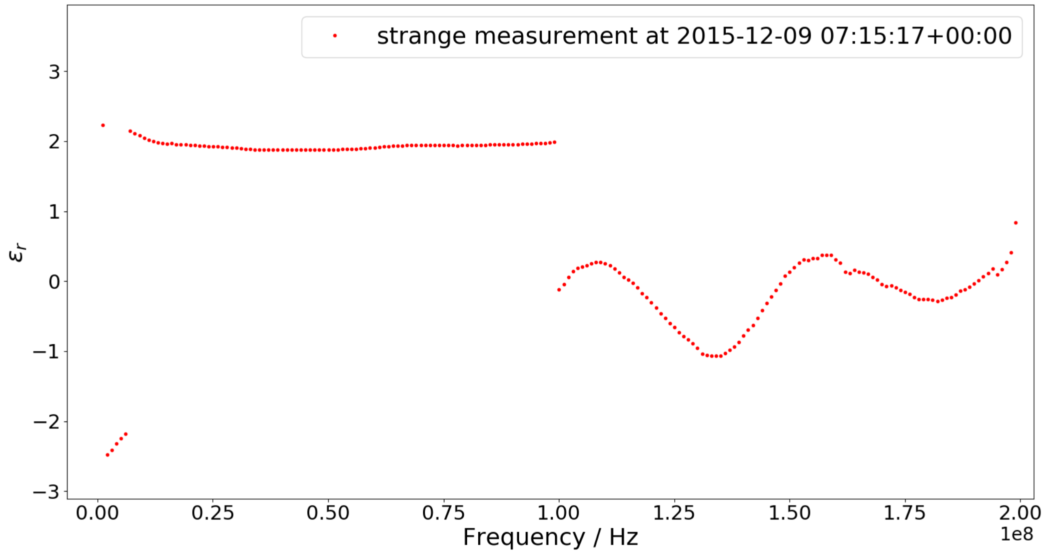

Figure 12: A behaviour similar to the one in Fig. 10 is visible. The range of regular data is larger.

the grapical user interface gives an impression of the procedure of measurement. The VNA starts at the low frequencies, measures the requested quantities and afterwards increases the frequency. If the battery of the VNA did not charge properly, it could be that there was just enough power for producing the signals of the first frequencies. At some time and frequency the VNA did not produce a signal of regular amplitude anymore, but still acquired the quantities. Next, the oscillating is caused by the calibration, as it reads the reflected and transmitted signal and rescales it by variables of the calibration file. This claim is supported by the fact, that the amount of frequencies measured regularly seems to be dependent on the time of day (Fig. 13). At night, the malfunctioning happens earlier than at day. Something like a dirty solar panel would negatively affect the charging of the batteries, but is still unequal zero. So at daytime the battery charges just enough to produce a few signals. However, the battery charge is not present, so the hypotheses cannot be tested. The raw data like the signal amplitude is already converted. It is also unclear what caused the VNA to appear to work normally again. A record of maintenance of the AERAWS could not be found. The regular looking days of part II still have features, that differ from part I. Their absolute values and variability are smaller. It is unclear, if this is a cause of the weather conditions or a malfunction.
Nonetheless, the measurements at the beginning are clearly flawed. The measurements do not fit the expected results, which points to an operating error, most likely caused by the power supply. The following datasets appear better, but still atypical. Hence, part II of the records is not trustworthy and will be ignored in the following analysis.

After five months of no recording, the VNA was replaced on 30th November 2016. This

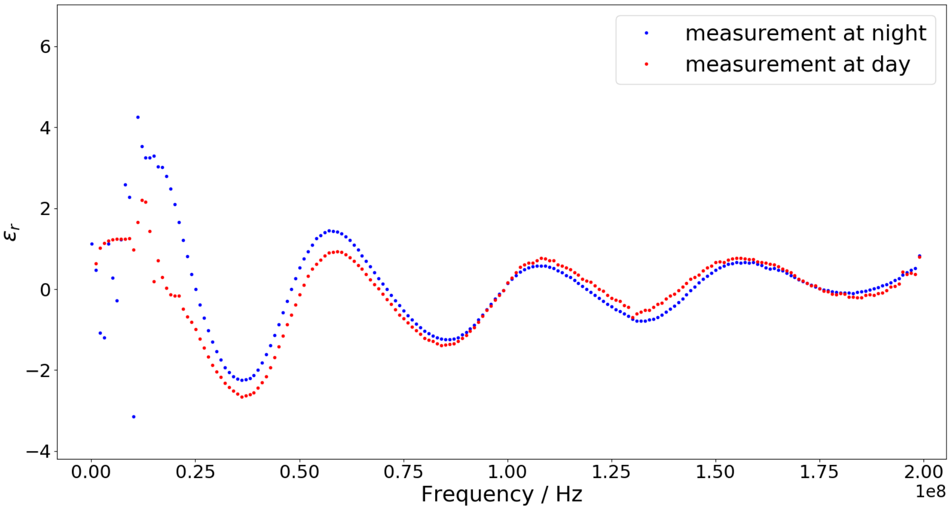

Figure 13: A day/night dependence is visble at the beginning of the measurement. The red points seem regular up to 10 MHz, while the blue points do not seem regular at all.

marks the beginning of **part III**, shown in Fig. 14.

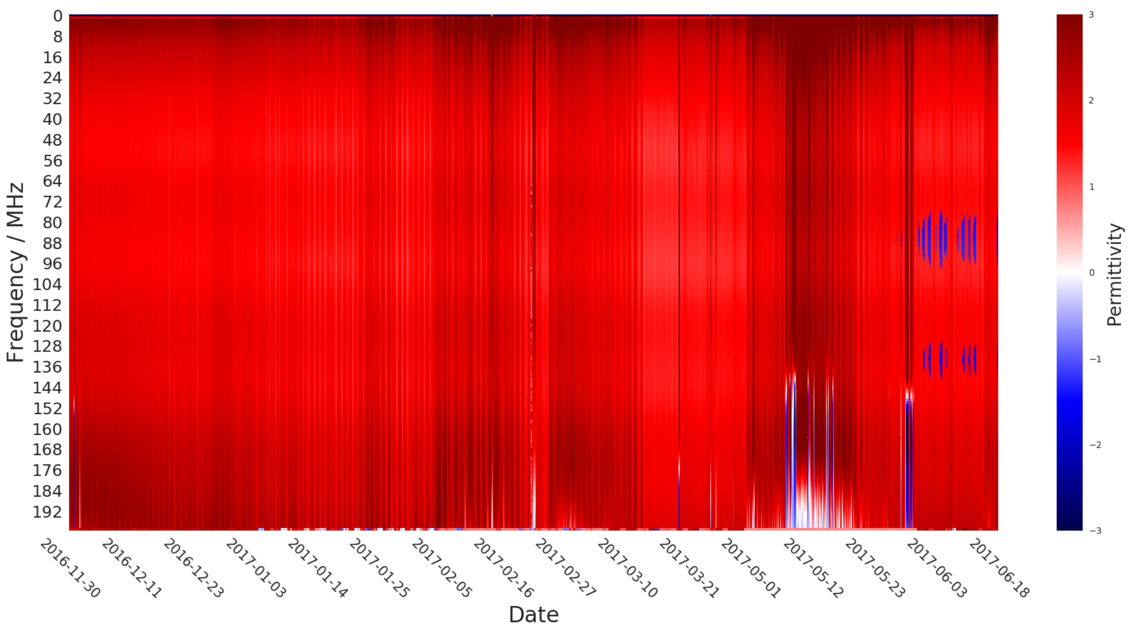

Figure 14: Zoomed part III of the heatmap in Fig. 8.

At first sight, the resulting data looks promising. The baseline of the values is comparable with part I. Furthermore, the variability looks fine. Occasionally, irregularities in the measurements occur, which, again, are most likely caused by insufficient power supply. Investigating the dataset deeper, a familiar feature can be identified.
As already mentioned, the new VNA was not calibrated, or being more specific, the VNA uses the calibration file of the old one. As a consequence, an oscillating behaviour just like previously discussed is visible, but the datapoints do not oscillate around zero anymore.

The VNA rescales the quantities dependent on frequency, too high or too low for different frequencies. This is visible in Fig. 15.

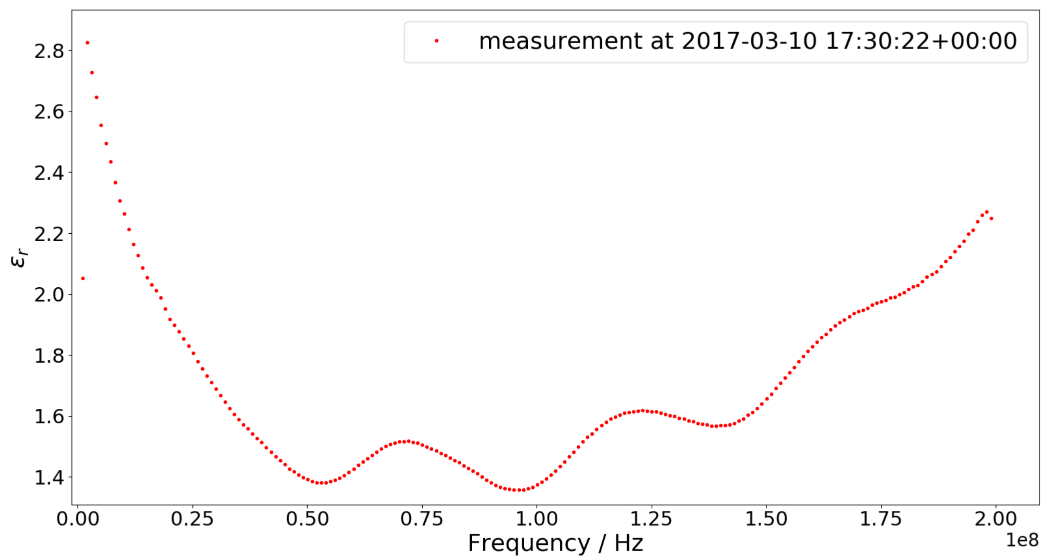

Figure 15: The plot shows the occuring oscillation around the expected model (see chapter for the discussion of the model) for the permittivity.

As will be explained in the next chapter, the absolute value could be wrong, but time dependencies should be visible. Therefore, part III will be used in this analysis.

Part IV starts on 18th June in 2017 at 15:15. The starting time can be determined that precisely as the value of the permittivity drops sharply at this measurement. More concretely, at 58MHz the value at 15 o'clock is $\varepsilon_r = 1.46$, the next measurement returns $\varepsilon_r = 0.89$, with the following datasets being of the same magnitude. Beside the drop of the values, a significant increase in the amount of negative values is visible (Fig. 16). The reason for these values is the phase angle of the impedance, which is needed in formula 3. Figure 17 shows the phase angle for a typical measurement of part I and IV respectively.

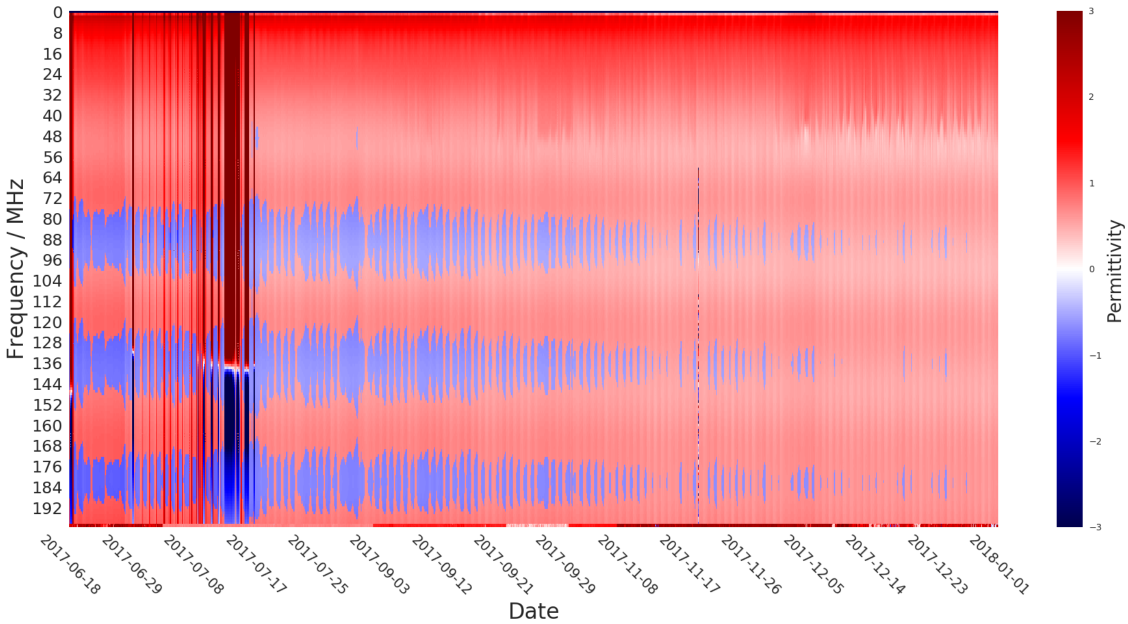

Figure 16: Zoomed part IV of the heatmap in Fig. 8.

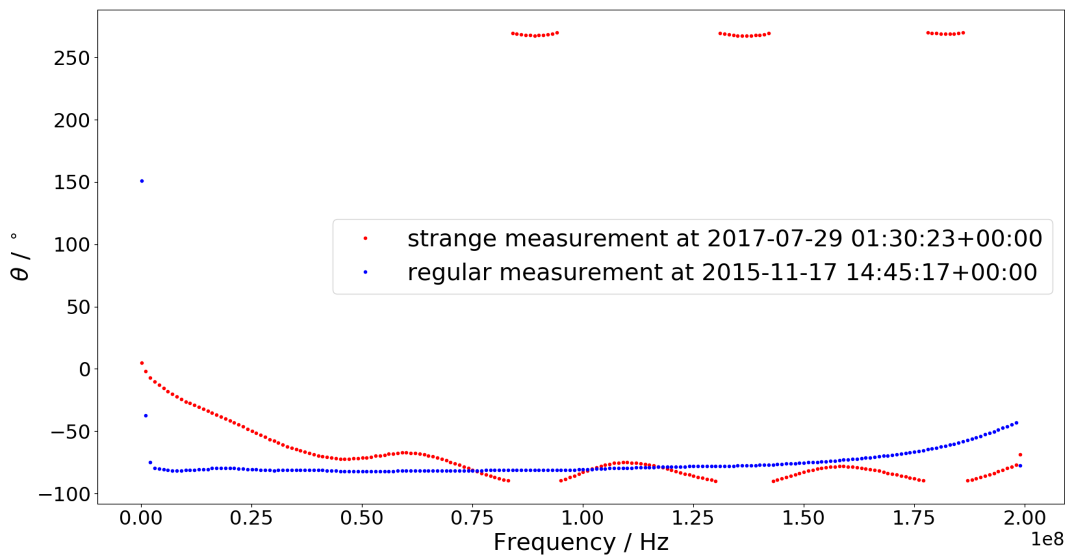

Figure 17: Comparison of different phase angle measurements; those from part IV show irregularities.

Two aspects are worth mentioning. Firstly, we still see an oscillating behaviour for the phase angle. The second and more obvious point is the jumps at different frequencies. One can see, as θ would drop below -90°, the angle jumps to 360° plus θ_- (θ_- is the phase angle if the value below -90°). This behaviour is a common feature when measuring the phase angle. As phase differences higher than 360° are possible, but only the shift from n $\cdot$ 360° is important, the angle makes a jump at some point. As a result, the frequency spectrum has to be unwrapped. It is done exemplarily in Fig. 18. Now the datapoints

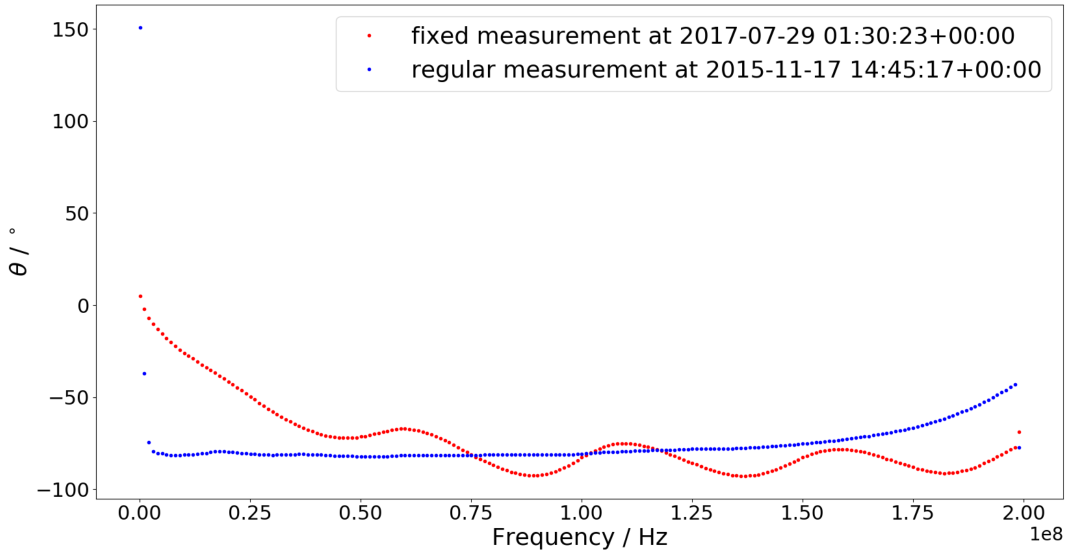

Figure 18: The unwrapping of θ is shown; the measurements are the same like in Fig. 17.

are steady. However, it does not solve the problem of negative values. As the tangens changes its sign when dropping below -90°, the solution to choose is taking the absolute value of the tangens in formula 3. Doing this, one gets a corrected heatmap. The corrected points fit optically, the applied method works. The plot appears smoother for part IV after correction, nevertheless, the low baseline is atypical and the oscillating is still visible. Additionally, the limited variation is striking. Especially the transition from part III to IV cannot be explained. Neither the VNA, nor the probe was changed. A damage of those components could occur in field and be an explanation. A connection to the weather, for example stormy conditions or extreme temperatures, could not be found. Hence, the conclusion is unclear. On the one hand, there seem to be small changes and, only watching part IV, it is consistent. On the other hand, the values are unphysical (<1). Even having the missing calibration in mind as a possible reason, it does not explain the big difference to part III, which, in turn, is consistent with part I. These arguments strongly disfavour using it for the analysis. In the end, part IV was not included for the analysis based on the presented points.
This decision is also based on the fact, that the cleaning or calibration of the data afterwards is challenging. The attempted methods are described in the following chapter.

4.3 Improvement of the data quality

4.3.1 Cleaning the data

As has been shown, the frequency dependent oscillation is most likely caused by an incorrect calibration, as this behaviour only seems to appear after the change of VNA. The probability for an artefact instead of a faulty measurement is rather low. Fixing this could

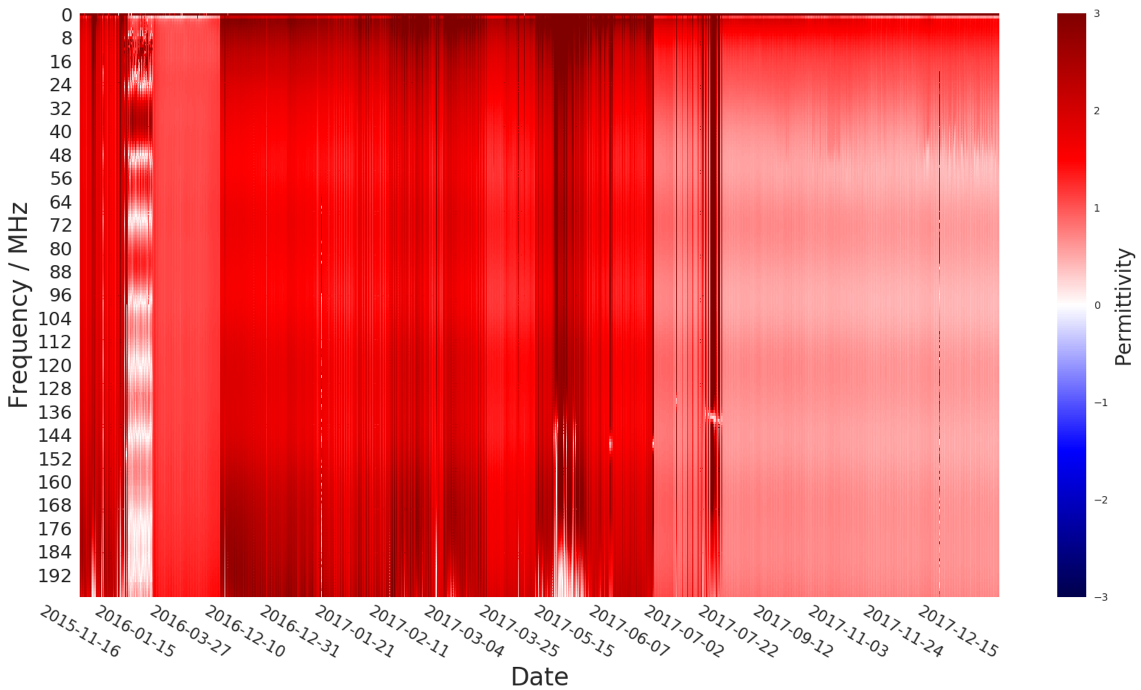

Figure 19: Heatmap, when using the absolute of the tangens

be done by editing the calibration file. As the file is a compressed bitmap, viewing and editing it in a text editor is not possible. No program was found to make the file readable. Another option is to look at the times when the calibration was recognisable? It was assumed that the strange measurements at part II were caused by an insufficient power supply. It could be that the produced signal is of zero amplitude. Then the spotted oscillation would just be the calibration, an individual offset for each frequency. If this is true, all permittivities should be same for the mentioned dates. As visible in Fig. 13, this is not the case. Therefore, the calibration must be dependent on signal height. The amplitudes of the signals are not equal to zero. Just a linear calibration without an offset is not possible either. The permittivities for amplitudes $\gg 0$ would be very large for some frequencies and almost 0 for other. As a result, the calibration cannot be determined from this data and, therefore, a correction through this method is not possible.
Another common way to eliminate unwanted oscillations is the discrete Fourier transform (DFT) and this possibility was discussed. At the DFT the n datapoints are depicted by a sum of n sine functions with different frequencies f_{DFT} (the DFT frequencies are not related to the frequencies of the measurement). In theory, the unwanted oscillation can be eliminated by filtering the associated f_{DFT} and then retransforming it. As it was tried, the best optical solution describing it, was filtering all frequencies except for one. Since, a single sine is not the model expected and also obviously not justifiable, this approach is not suitable. In addition, one has to be completely sure that the oscillation is a malfunction.

4.3.2 Proposing a model

Up to now, no useful model for describing the permittivity has been described. Nevertheless, having one could help to judge the quality of the data and eliminate faulty measurements.

It is easier to look at this problem with more basic data. The permittivity is calculated via the frequency, the impedance and its phase angle. The influence of the angle is comparably small. For example, consider a typical change from -89° to -85°. Inserting it into $f(\theta) = \frac{\tan\theta}{\sqrt{1+\tan^2\theta}}$, returns the result of $f(-89°) \approx 0.999$ and $f(-85°) \approx 0.996$. The impedance is the more crucial factor, shown in Fig. 20.

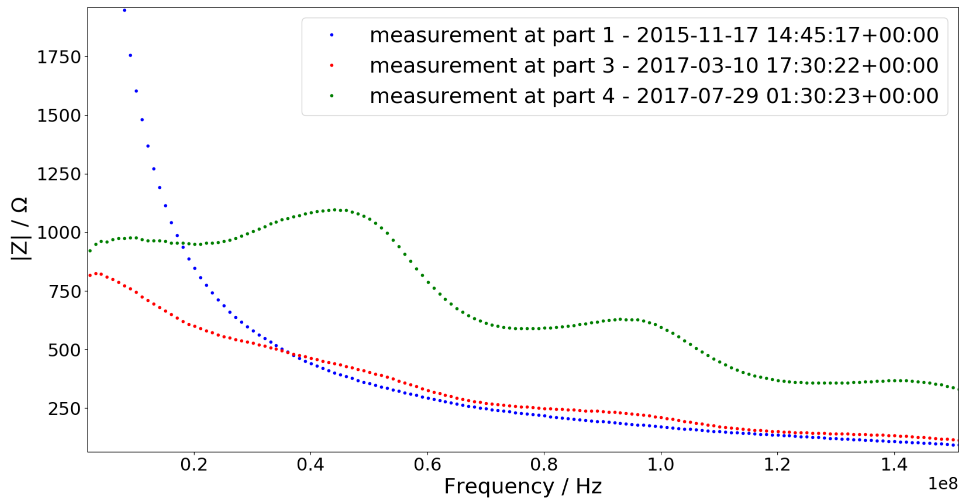

Figure 20: Typical developements of the impedance for the different parts.

The development of the shown blue points is similar to others from part I. The process looks steady and none of the points are inconsistent in the relevant frequency band and there are no outliers.

The dataset representing part III is similar, nonetheless there differences are visible. In particular below 30MHz, major variations in height can be observed. Furthermore, the presented oscillations are visible. Nearly the same decrease appears.

In contrast to this, the measurement of part IV is atypical. Neither the height, nor the decrease seem to be the same. Another striking feature is the oscillation, which is a multiple in amplitude compared to those from part III. As those irregularities cannot be explained and the discrepancies are severe, the decision to exclude the data from the analysis is affirmed at this point.

The physical model for the absolute impedance is

$$|Z| = \sqrt{(X_\mathrm{L} - X_\mathrm{C})^2 + R^2} = \sqrt{\left(2\pi L f - \frac{1}{2\pi C f}\right)^2 + R^2}, \tag{4}$$

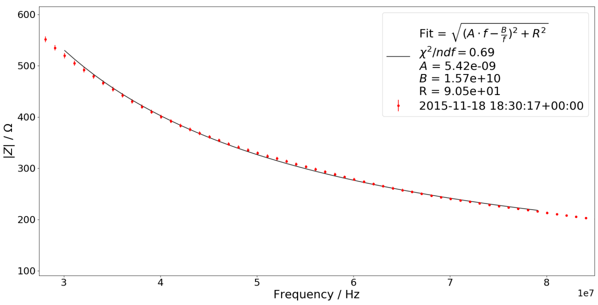

(a)

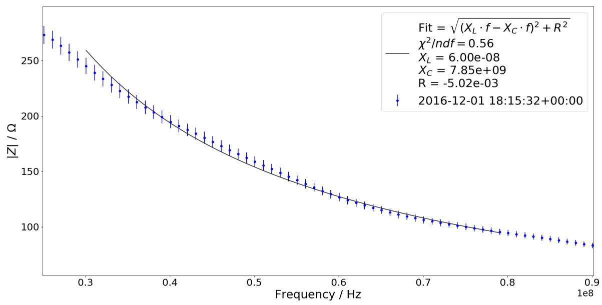

(b)

Figure 21: Two good examples for the fits are shown; left for part I, right for part III.

where $X_\mathrm{L} = 2\pi L f$ is the inductive resistance (L is the inductivity), $X_\mathrm{C} = \frac{1}{2\pi C f}$ is the capacitive resistance (C is the capacity) and f is the frequency. The model can be used to fit the data and test if they are consistent. A simple way to verify this is to check the fit parameter. It is worth mentioning that only the datapoints between 30 and 80 MHz, the relevant frequency band for AERA, are used for the fits. The errorbars are derived via the resulting reduced chi-square. They are chosen so such that the resulting reduced chi-square is approximately of the magnitude of one. The errors were set to 1% for datasets of part I and 3% for datasets of part III. This method has two advantages. The first one is that one gets an estimate for the error if the absolute height is correct. The second advantage is that the datasets can be compared. The chi-square is not meaningful if the model fit the data, as the errorbar is chosen by the chi-square, but it is significant which dataset fit better to the model.

Figure 21a shows an example from part I. Indeed, independent of the chosen errors, the fit describes the measured datapoints well optically. The same can be done for measurements of part III (Fig. 21b). The result of the oscillation is clearly visible for part III, the datapoints oscillate around the model. The result appears acceptable and the relation between chosen model and measurement is visible.

Figure 23 summarizes the output, after performing the fit for every dataset.

The significance of the plots will be explained now, starting with the first row (Fig.22a and 22b). It shows the distribution of the reduced chi-squares separated for part I and III. The distributions are dense and there are just a few outliers, a small percentage in total. But those are the interesting ones. First considering the fits, for which the reduced chi-squares lay at the right edge of the histogram. Obvious for part I, and also recognizable for part III, the fits still describe the datapoints. Nonetheless, deviations, small for part I and larger for part III, are visible. As can be seen in the plots (Fig.22c and 22d), even these bad fits are acceptable and can be used.

Figures 22e and 22f show the fits with high reduced chi-square, those not visible in the histograms. The reasons for those bad fits can be easily determined. For these measurements, an internal error (see again chapter 4.2) occurs and distorts the dataset. The datasets influenced by the malfunctioning can be determined and excluded from the anal-

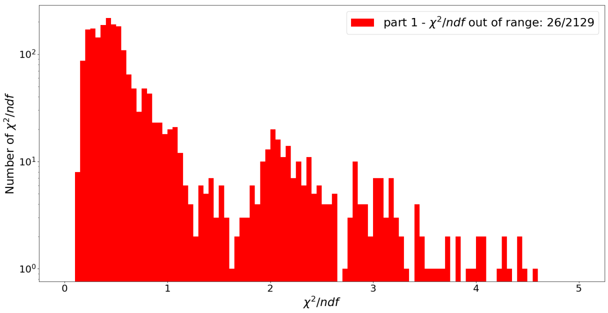

(a) Distribution of the chi-squares for part I.

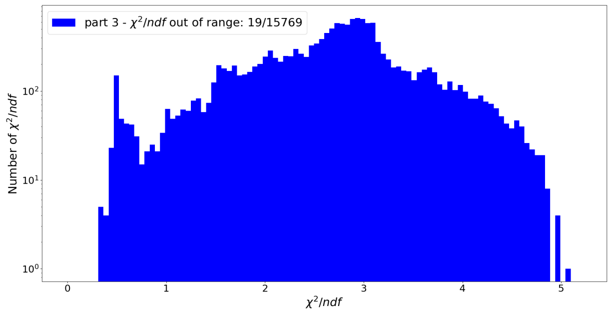

(b) Distribution of the chi-squares for part III.

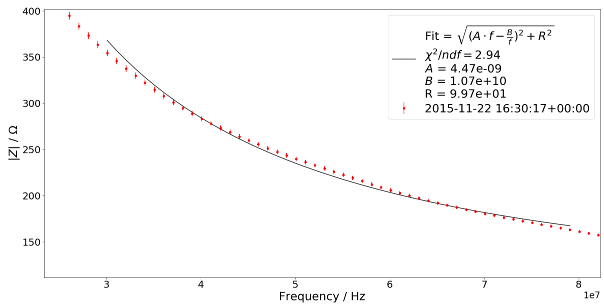

(c) Example of a fit for part I with slightly increased chi-square.

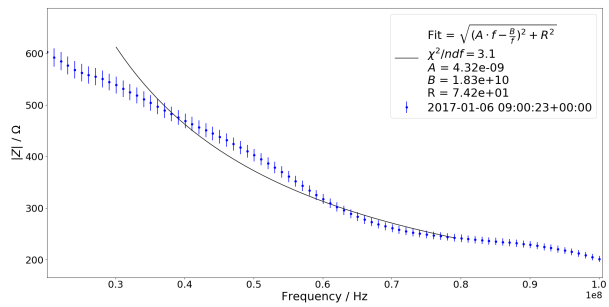

(d) Example of a fit for part III with slightly increased chi-square.

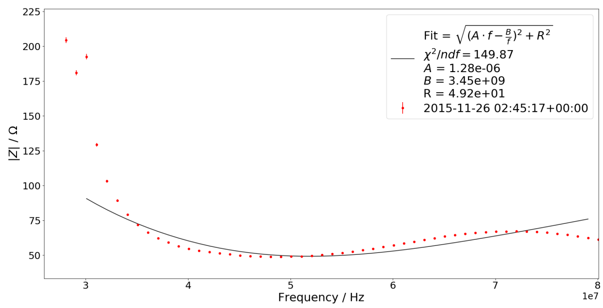

(e) Example of a fit for part I with large chi-square.

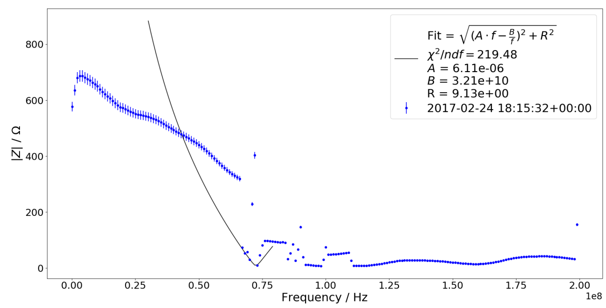

(f) Example of a fit for part III with large chi-square.

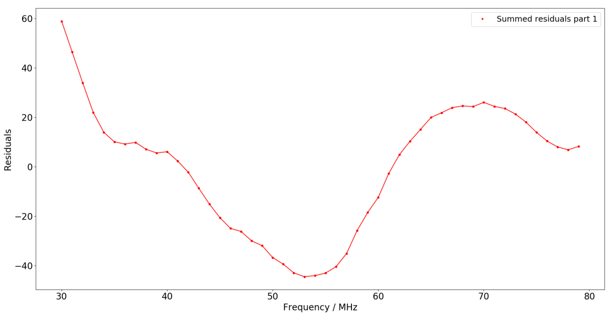

(g) Summed residuals of the fits for each frequency of part I.

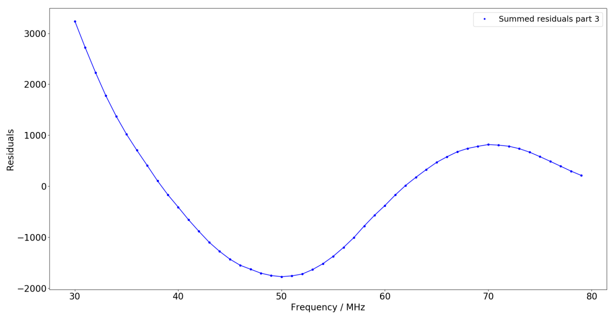

(h) Summed residuals of the fits for each frequency of part III.

Figure 22: Distribution of the chi-squares and residuals and different examples for the fits are shown.

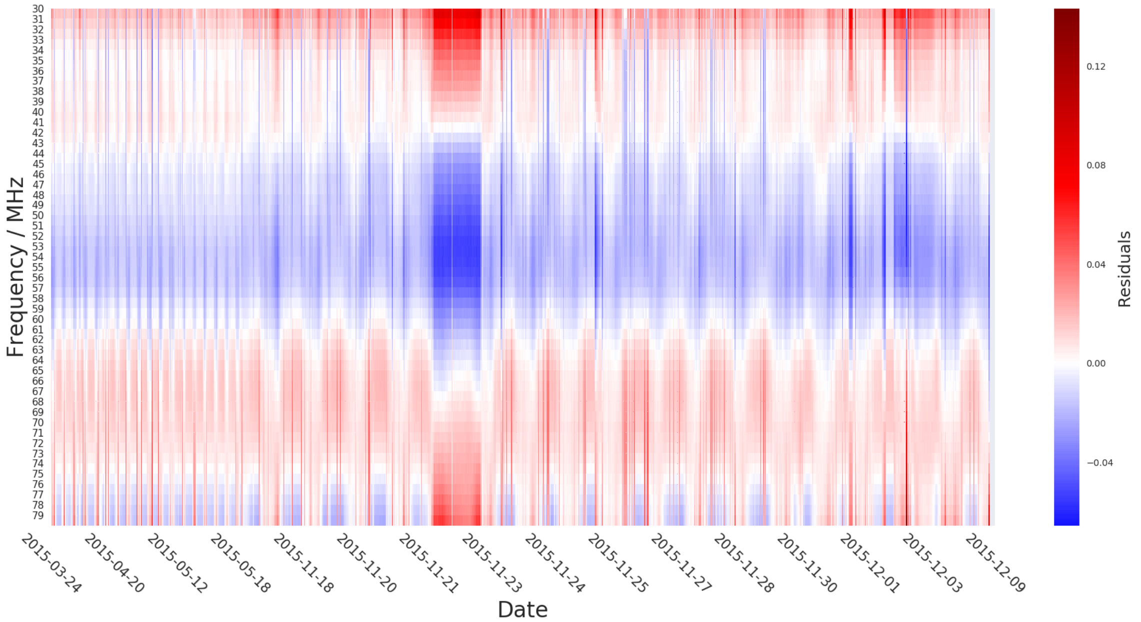

(a) Fit residuals for part I are shown.

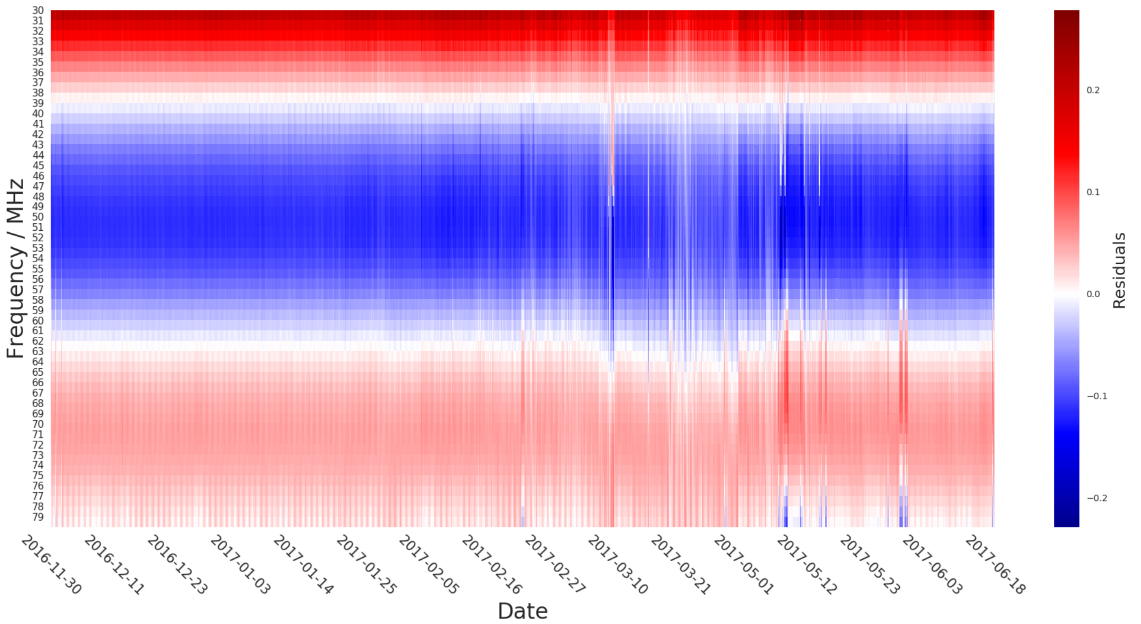

(b) Fit residuals for part III are shown.

Figure 23: The plots show the residuals of the fit; there are three frequencies for part I and two frequencies for part III visble with minimal residuals.

ysis.
The last four figures show the deviation of the datapoints from the proposed model. These plots cointain two important pieces of information that should be described. The first one concerns the frequency dependency of the residuals. It seems as if the fit matches the datapoints at some frequencies better than at others. For part I, the sum of all residuals (Fig. 22g), as well as every single residual (Fig. 23a), is nearly zero for three frequencies. Two of these frequencies match with those of part III: 38MHz and 62MHz. On the one hand, it could mean these frequencies are nearly free from systematical and statistical errors. If this is the case, the mentioned frequencies would be prefered for the analysis. This is only the case if the model is reliable. On the other hand, it could be biased and be a mere artifact. Then it would not have any advantages with respect to other frequencies. Up to this point, the oscillations were only seen for measurement coming from part III or IV. Looking at the heatmap in figure 23a, the residuals also seem to oscillate around the model. The amplitude of it is not as high as for part III, nevertheless, they are existent (note the differents colourscale). There are a few possible explanations for this behaviour in part I.
Firstly, the assumption made until now, that the wrong calibration is the cause for the oscillation, could be wrong. Two new possibilities appear. First, the oscillation could be an internal error and VNA specific. The other option is that there is an outer systematic cause like noise in some frequency bands. This does not explain why the residuals for part I are nearly zero for three frequencies and for part III just for two.
Secondly, the assumption could be validated by this feature. If the calibration is not perfect, for some (or all) frequencies a systematic error remains. As this misfeature looks similar for part I and III, mainly differing by the height, it is likely to be caused by the same reason.
As already mentioned before, the raw data, needed to confirm or negate this assumption, is not given. Hence, the features of the plots are just hints pointing to a cause. Nevertheless, the work done is not useless and the following conclusions can be drawn:

- Fixing the corrupt data is challenging and would most likely go beyond the scope of this thesis. Hence, part II and part IV of the data are not used in the analysis.
- The calibration is probably causing the mentioned oscillation.
- A model for the impedance and, therefore, for the permittivity is proposed.
- Some records are broken through a malfunctioning of the setup. They can be identified using the model. They are excluded from the analysis.

Table 2 summarizes the number of data points rejected and used for analysis for the different parts.

Table 2: Overview of the used data

Part	I	II	III	IV
Days	267	329	200	199
Raw datasets	2129	3419	15769	12648
Rejected datsets	26	3419	19	12648
Used datasets	2103	0	15750	0

In this section, obvious data errors were discussed. The absolute value of the permittivity was not questioned. This will be discussed in the following chapter and compared to literature and an additional measurement at the Pierre Auger Observatory.

4.4 Comparison with another measurement at the Pierre Auger Observatory

The measurement of the permittivity at the AERAWS is not the only one performed at the Pierre Auger Observatory. In [2] a capacitor was used to measure the permittivity through the capacitance of the plates with soil of the observatory between them. As part of the thesis in [2], two investigations were made.
First the dependence of the location was investigated. The soil composition at the observatory and at AERA is strongly variable location dependent. Westwards in AERA, the ground becomes more and more sandy and the permittivity decreases. In the measurement, permittivities up to 8.1 in the east and about 5 in the west (weighted median of the frequency band 30 - 60 MHz) of the AERA field were determined. The nearest measurement to AERAWS shows a valueof ε_r =6.5. Taking this as the reference value, a rather large difference is visible to the measurement in [4]. In the frequency band from 30 to 80 MHz, no value of this height is observed. The maximum is around 5, and the baseline is approximately 1.6. From [16] it is known that the measurements were all done in one day. The days before were rainy and the soil was still moist. As a consequence, the results could be unnaturally high.
To control for wetness, a second measurement was carried out. A jar of the soil was taken to a labotory and sand was dried. The permittivity was measured for different degrees of humidity of the soil. The results given in Fig. 24 show values between 2 and 10, increasing with soil humidity. Since the permittivity is increasing both going eastwards and with humidity, the value expected for the soil at the AERAWS is clearly above 2, and thus is contradicting to the measurements presented here.
The literature [12] is more consistent with the measurement and values of [2]. There also are two additional arguments to support this choice. The first depends on the type of measurement. The datataking in [2] was always made while someone was present. Hence, some outer influences like a false configuration or a lack of soil sample can be ruled out.

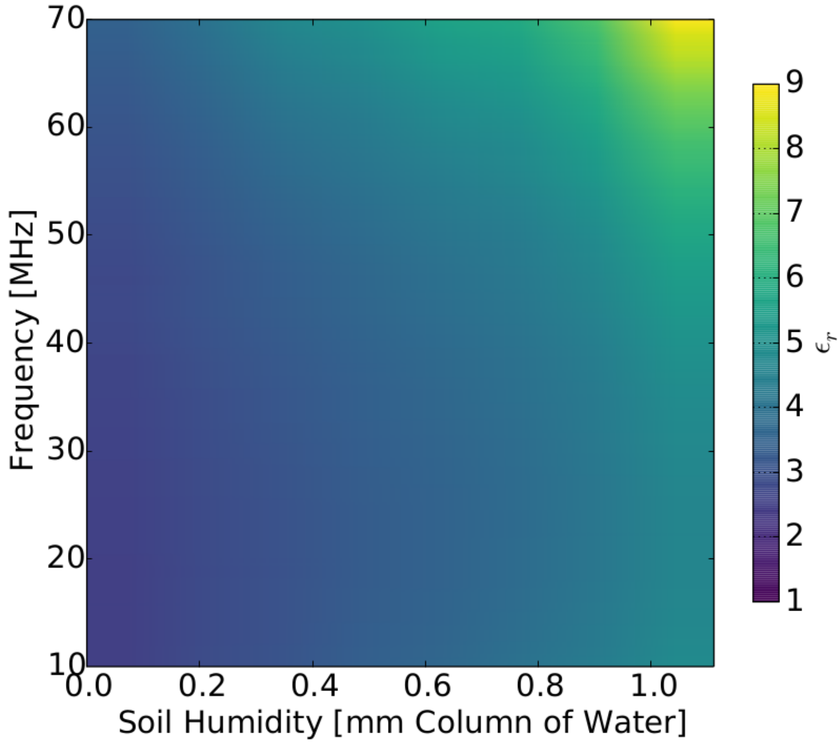

Figure 24: Dependency of the permittivity of the humidity measured in [2].

For example, sometimes the soil could be removed by the wind from the probe and this would not be noticed at the AERAWS. The other argument concerns the preparation of the measurement. The measurement in [4] includes much work. Nonetheless, the measurement in [2] seems more carefully arranged. For example, the setup was tested with differents mediums, for which the permittivity is known. The test measurements are in line with to literature, so the method with a capacitor works. In constrast, in [4], a calibration and several test measurements were made but the results were inconsistent and the test medium (wet grass) could have been chosen more carefully.
As a conclusion, the measurements in [2] are more trustworthy. The results in [4] seem too low in magnitude. Nevertheless, the data is useful. As this thesis focuses on the change of the permittivity, the absolute value is of secondary importance. If there is a missing factor or offset, it does not influence the trends and effects.

An additional aspect is the expected error. Up to now, the permittivity has been plotted without errorbars. They will be omitted in further plots for the following reason. In [4], the statistical error was determined to be < 5 %. The systematic error was supposed to be negligible after the calibration. As can be seen, neither the calibration was functional, nor are the deviations explainable by. The only remaining estimate is the maximal error. As this would have huge variation, the quality and significance would not increase. The errors would even be greater than the values themselves and make the plots indiscernible. For other quantities shown in the plots to follow like humidity, the errors would also have

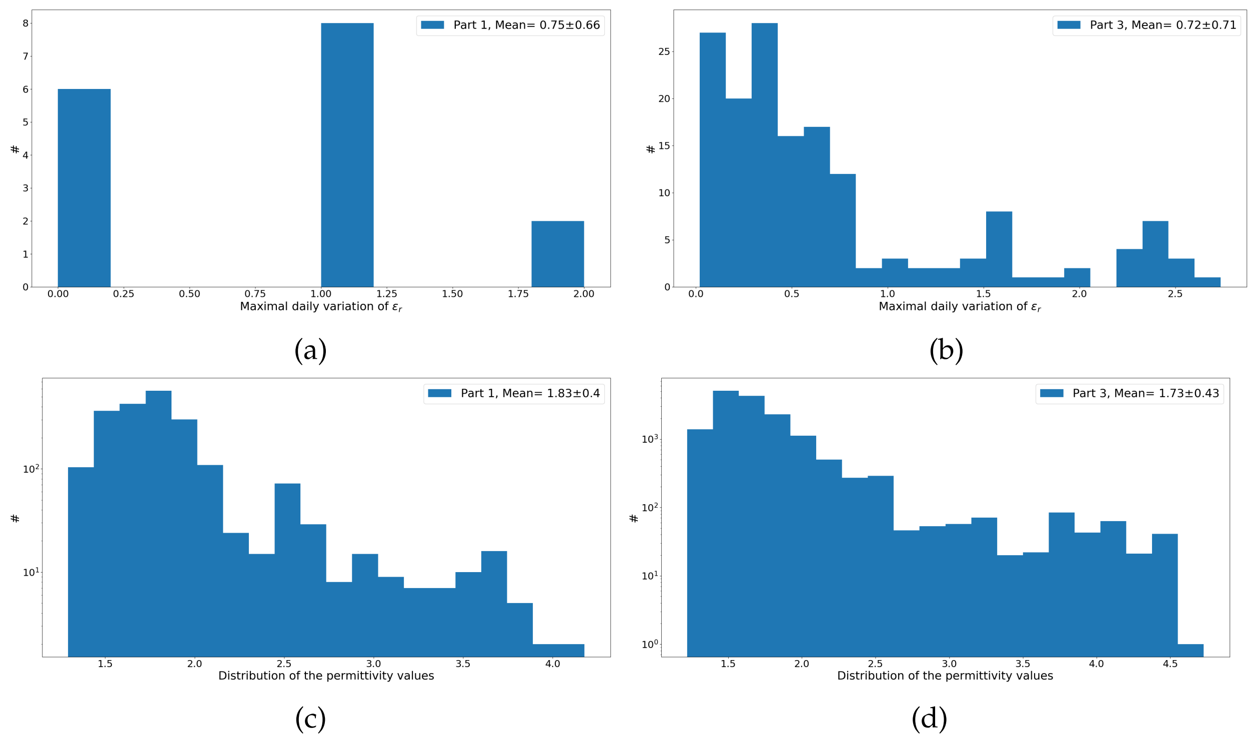

Figure 25: **(a)** and **(b)** show the distribution of differences between the maximal and minimal value for the day; all days with more than 90 data points are taken into account. **(c)** and **(d)** show the distribution of the permittivity for all measurements.

to be estimated. In comparison to the permittivity, those errors would be negligible. Thus the error is also not plotted.

4.5 Variation of the permittivity

Independent of the absolute values of the measured permittivity, the variability of the permittivity transfers to a systematic uncertainty of the AERA sensitivity. For an estimation of the variability, the difference of the maximum and minimum of the permittivity for one day is shown in Fig. 25. The calculated errors are the standard deviation of the mean, the systematic and statistical error is not considered. and statistical error is not considered The distribution in Fig. 25a looks strange due to a low statistic. Figure 25b is more significant, most values are below one. These variations are caused by statistical fluctuation and weak effects like the humidity and temperature (chapter 5.2). Increased variations are correlated to stronger effects like the rain, which causes large rises in the permittivity. The median of the variation for part III is 0.47, compared to a mean of 0.72 $\pm$ 0.71.

Figure 25c and 25d summarize the distribution of the permittivity values. The mean for part I is 1.83 $\pm$ 0.40 while the median is 1.77. The values are smaller for part III. The mean is about 1.73 $\pm$ 0.43 and the median is 1.61.

The majority of the values for the permittivity and variation are small, only a small amount of measurements show permittivities > 2 and variations > 1. So, the causes for large values are rather rare. One also can see that the mean and median for part I is greater than for part III. This is caused by the different measurement periods. Part I was mainly measured in Argentinia summer, when the temperatures and the humidity is higher and heavy rain is more likely to occur. Figure 26 shows the distribution of two exemplary days. One rainless day which shows basically no variation in the permittivity and another rainy day, that shows a wide distribution of values.

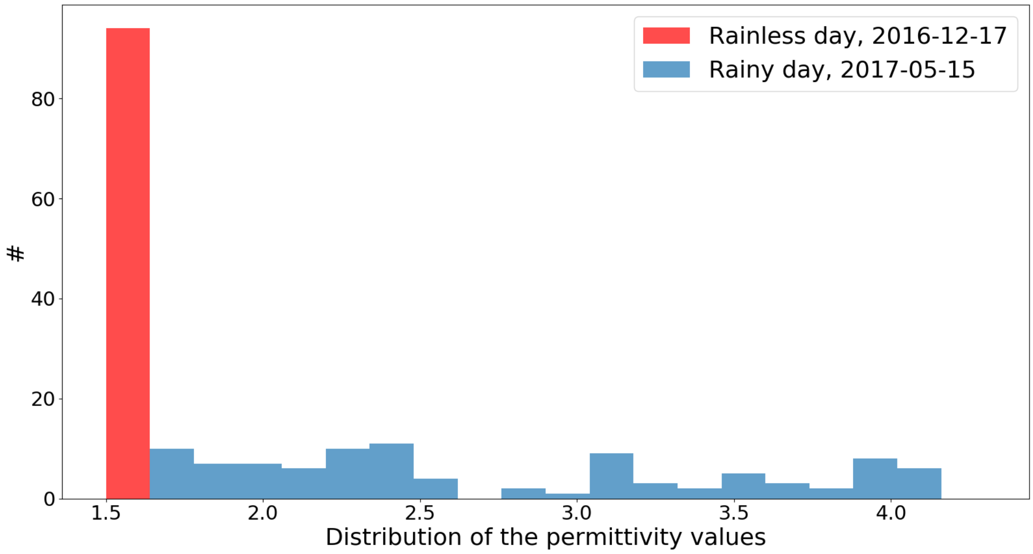

Figure 26: The plots shows the distributions of the permittivity values for two days, a rainless day (red) and a rainy day (blue). For the rainless day all measurements are within one bin. The chosen days are representative for rainy and rainless days.

5 Enviromental influences on the permittivity

Up to now, this thesis has focused on the data quality dependent on the setup. The actual analysis should be brought forward and the different external influences should be investigated. Before doing this, it has to be discussed which parameter could influence the permittivity that is recorded at the observatory.

5.1 Measurements of weather dependent parameters at the Pierre Auger Observatory

There are several stations at the observatory recording different enviromental parameters. An important aspect correlating those parameters is the distance between the permittivity setup and the station measuring the parameter. Therefore, the station with lowest distance is always chosen.
As mentioned before, AERAWS is connected to the setup and the distance between the equipment is less then 5 m. The big disadvantage using the data of AERAWS is that there is no useful data at all. As the station was moved to the current location, it was not mounted properly, due to missing and unsuitable connectors. The only quantities measured are the average windspeed and the pressure.
The second nearest measurement is the weather station at the central radio station (CRS) with a distance of about 1.5 km. The issue about missing data at the AERAWS is well known, the station of the CRS was favoured before the beginning of the thesis. Issues about data acquisition were not reported or known. While parameters, like temperature and hydrometry, are well logged, the rain precipitation data registered only zeros starting the 17th of February 2015. Right after midnight of that day, rainfall began, the heaviest since the begin of measurement in 2010 with 145.9 mm per hour at its maximum. Afterwards, the precipitation declined regularly until it reached zero. From this time on, no rain was measured again as well as no hail (same sensor). This is definitely a malfunctioning of the sensor. The cause cannot be identified. All other measurements (wind, temperature, pressure, hydrometry), which are acquired by the same setup, continued their recording as before. They also use the same signal and power cable as the rain sensor. Therefore, the rain sensor itself has to be defect. A damage caused by the amount of rain is unlikely, since the limit for precipitation is stated to be 200 mm per hour [17]. Another type of damage can be triggered by lightning. Looking into the measurements of lightning, there was, indeed, a thunderstorm. But relying on the data of the Pierre Auger Observatory, the lightnings did not hit the CRS or the surrounding area.
It can always happen, especially for this amount of rainfall, that some water flowed into the sensor causing a short circuit.
It is unlucky that the acquisition of rain stops about one month before the permittivity setup was mounted. As a result, there is no overlap. Nevertheless, temperature and hy-

drometry can be used for the analysis.

Another option are the weather stations at the FD buildings. As the telescopes are very sensitive, they have to be protected from rain. The rainfall causes the closing of the shutter of the FD building. Looking into the database, the sensor for it is logged. Unfortunately, the measurement is just a bool value. So, the time when it rained at each FD is known, but not the amount. The same issue would appear for the two laser facilities from earlier measurements, but those are not even logged.
Other measurements are not known. The next idea is to get data from institutions not associated with the observatory. As a public and free source, the airport provides its measurements. They can be downloaded [18] and contain the precipitation. The disadvantage is the rather large distance with more than 40 km.
The city El Sosneado is one tenth of this distance away from the AERAWS. The weather station offers its data of the last 30 years including the precipitation. As it is only recorded on an hourly basis and the data is not freely available, the data was not purchased.
The correlation with the rain becomes rather difficult through this lack of data. Nevertheless, it should be tried. But first, the impact of temperature and humidity is investigated.

5.2 Daily variation of the permittivity

Looking at time dependent variation of permittivity, the value of 38 MHz is chosen. Using the proposed model this was found in chapter 4.3.2 to be one of the frequencies best described. Other frequencies were tested for comparision and gave equivalent results.
Figure 27 shows the developement for ten days in December 2016.

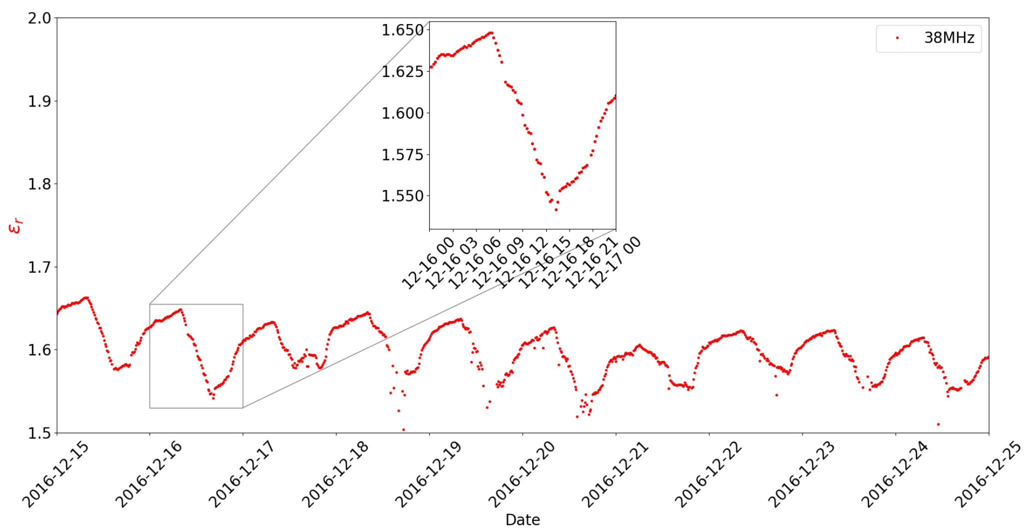

Figure 27: The time developement of the permittivity at 38 MHz for 10 days in December 2016 is shown; the timezone is UTC time.

The developement of the permittivity is steady except for a few outlayers. A periodic

development is visible, with its maximum around 5 am and minimum at 1 pm local time. This phenomenon can be explained by the effect of morning dew. In the evening it gets colder, the relative humidity increases. Partly it condenses and accumulates as water in the soil. Therefore, the permittivity rises. This process is maximal for low temperatures at the end of the night.
That way, the moisture of the soil and therefore the permittivity is related to the humidity. This can also be seen in Fig. 28. The developement of the two parameters is shifted by about one to two hours. The processes are not instantaneous and there is a difference between soil and air humidity.

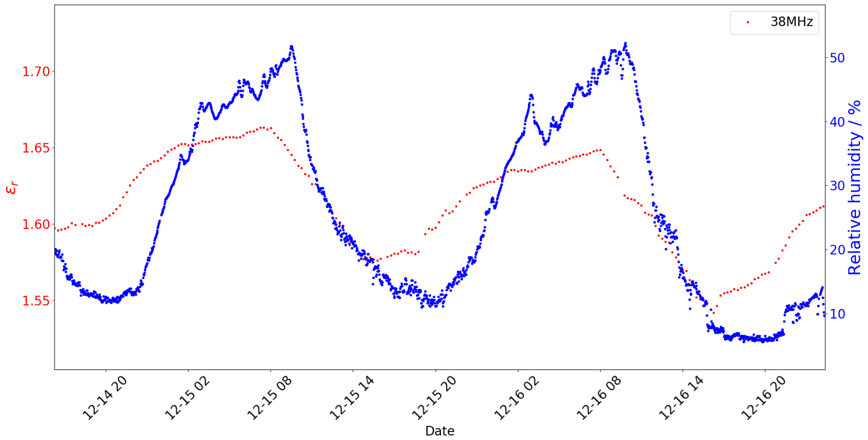

Figure 28: Daily variation of humidity and permittivity is depicted; the small time shift of the maximums and minimums can be explained the differentiation between soil and air humidity. The air humidity lags behind the permittivity, since the soil humidity is affected first by temperature changes and the permittivity is dependent of the soil.

The variation of the permittivity caused by the air humidity effect is less than 10 %, mostly times around 4 %.
The correlation coefficient is calculated and the correlation is depicted in Fig. 29. The coefficients with 0.24 for part I and 0.32 for part III are comparatively low. It is visible that many datapoints seem to be on a line with a slight slope. Through different offsets, the result would seem uncorrelated, just like in the plots. As precipitation has greater impact than the humidity of the air on the soil moisture, one would expect rainfall dominates the correlation. To eliminate this influence, one has to look for days, on which rain was unlikely to occur. Hence, the calculation is repeated for the aforementioned periods. Indeed, the correlation coefficient increases for a finer time scale. The correlation could be improved further by including the shift mentioned in Fig. 28.
A inversed development can be seen for the permittivity and temperature. The temperature reaches its minimum while the permittivity is maximal. In the morning, the temperature rises and the permittivity drops again.
The correlation with the temperature is caused by the rise in the humidity in this case. As mentioned in section 3.2, a direct correlation should also be visible. Nevertheless, this

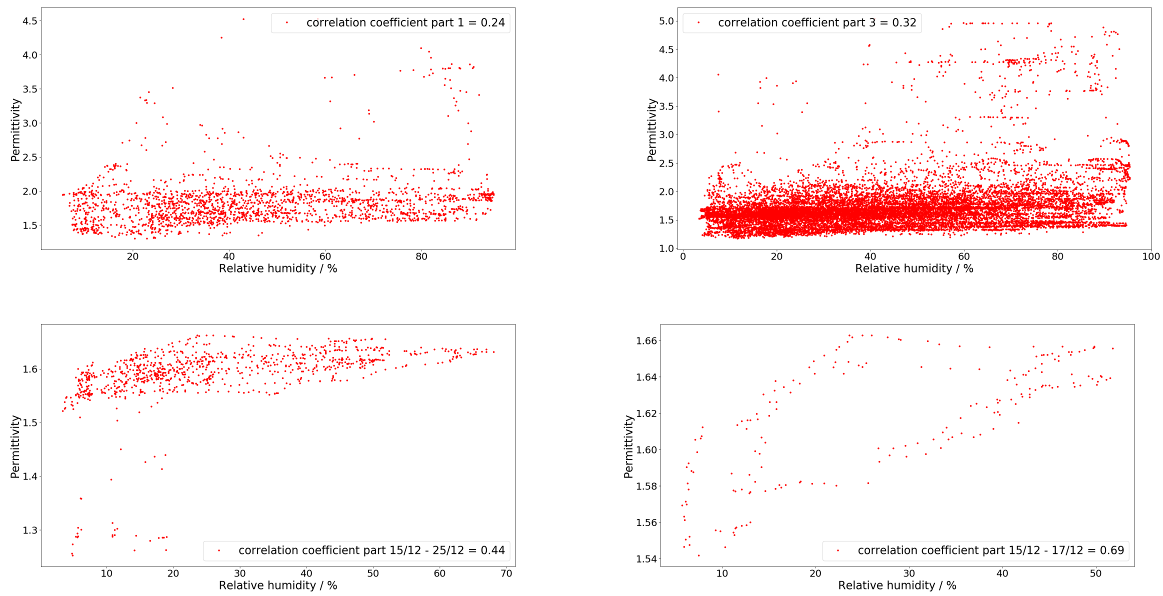

Figure 29: Correlation between the humidity and permittivity; at the top left the correlation is shown for part I, to the right for part III and below are correlations for 10 days (left) and one day (right) of part III visible.

effect is rather weak and is supressed by other phenomena. Attempts to eliminate those, by selecting rainless days and just using times when the humidity was in a certain range, influenced the correlation only slightly. The coefficients are negative and the largest value absolutely is less than 0.4.

5.3 Correlation with raindata from the Malargüe airport

The precipitation is only known by the data from Malargüe airport. Data is taken in 3 hour cycles and the precipitation is summed up for this time. In addition, the average winddirection is given. A disadvantage is the distance of more than 40 km. Therefore, a coincidence with the wind direction should be regarded. The airport is directly south of the observatory at an angle of about 3°. So the permittivity should have a maximum before the precipitation at the airport if the wind blows from the north. After the rainfall, if the wind direction is northward.
The period of time before and after was chosen to five hours before or after the rainfall. Additionally, wind directions from east or west were also observed, there the maximum was chosen from the five hours before and after. The result is shown in Fig. 30. It is only shown for data from part III. There is just a small amount of precipitation in the time of part I and the result is not significant. No correlation is visible at all, independent of the wind direction. Other time spans did not improve the correlation significantly. Most likely, the distance is too large and the devolepment of the clouds cannot be predicted that easily.

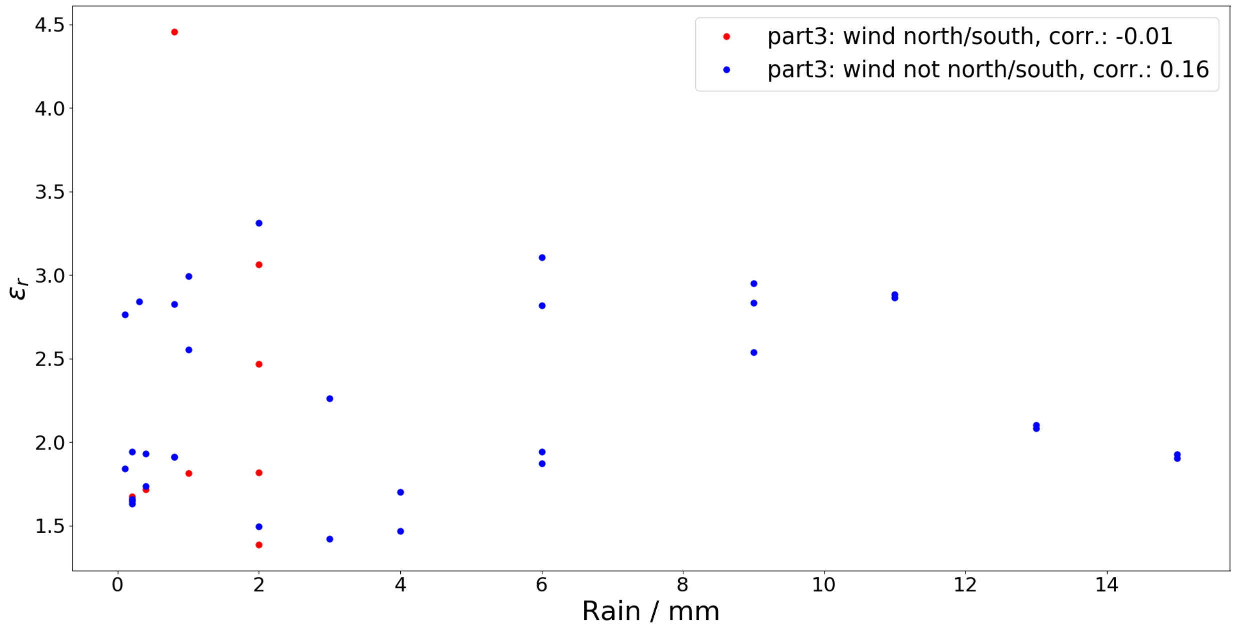

Figure 30: Correlation between precipitation at Malrgüe airport and the permittivity, the distance is too large for visible effects.

5.4 Qualitative description with FD data

The data from the airport does not seem to be useful, but it gives information on the amount of rain. There are four FD buildings (the FD 'HEAT' is approximately 100 m next to 'Coihueco'and therefore not considered separately), each at a different distance from the setup, which measure if it rains without the amount of precipitation. The data allows to correlate the rainfall and the permittivity.

The major advantage is the amount of data, with four independent measurements and locations. They register all changes, e.g. when it starts to rain, the bool value changes to 1. The locations of the FD stations and their distances to the AERAWS are shown in Fig. 31. The FDs surround the field of AERA. Hence, the probability is given, that if it rains at the AERAWS, it also rains, with some time shift, at one of the FD facilities. Instead of directly correlating rain precipitation with permittivity, here the idea is to check in case of strong changes if the permittivity correlate with events of rainfall. Clearly, only qualitative statments can be done this way. The outcome resulting from this method can be seen in Fig. 32 and 33. The colorbars represent each FD and the time when it rained. Plots for the frequency of 38 MHz are shown, the plots for other frequencies are similar and the variations stated are of same magnitude.

There are a few features to mention in the different plots. The first two pictures are examples of a direct correlation between the rain at the FD buildings and the increase of the permittivity. In the beginning, except for some minutes, only distant FD stations far off indicate rain and no rise in the permittivity can be seen. Afterwards, longer periods start when the close FD station Coihueco registers precipitation. The permittivity rises from approximately 1.55 to more than 1.8 in just 15 minutes. That is a relative rise of about

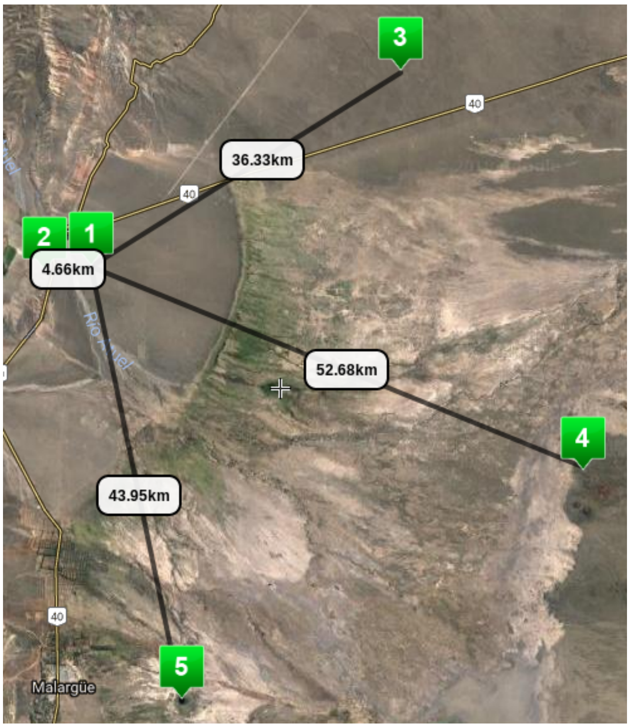

Figure 31: Map showing the FD sites and AERAWS: 1 AERAWS, 2 FD Coihueco, 3 FD Loma Amarillo, 4 FD Los Morales, 5 Los Leones. Picture from [19]

20 %. Even as the rain stops, the permittivity stays at this height.
The following graphic shows a similar behaviour. Two sharp rises are visible, both are especially related to the data from Coihueco. At this time, it seems like it was heavily raining at the region of the observatory. A quick comparisin with the data from the airport confirms this, as the precipitation was rather high at that time. The result is a rise by approximatelly 130 % relatively and 2.25 absolutely. The peak is of large width, statistical fluctuation or single false measurements can be excluded. The end of the peak is unexpected. It drops abruptly, the same way it rises again for one hour. The following explanation is possible. The maximum height of the permittivity is only reached if the soil is wet and not just moist. The water drains into deeper layers of the ground and does not influence the measurement anymore. After the fall, the rain starts again. At least a small green bar is visible one hour before the rise. After the second drop the variation stops and the baseline is higher than before the rainfall. Now the soil is not wet anymore, but still moist.
A continuation of this situation can be seen in Fig. 34. After rainfall at the beginning, the value of the permittivity is slightly increased. The following fluctuation is caused by the before described effect of the humidity. More significant is the visible slope. The baseline is about 1.8 at the beginning and decreases in two weeks to 1.3. This could be caused by the evaporation of the water in the ground, the soil gets dryer each day.
One can see that most of the peaks can be explained by this method. However, there are datasets, which show the disadvantages of the method. This is shown in Fig. 35.

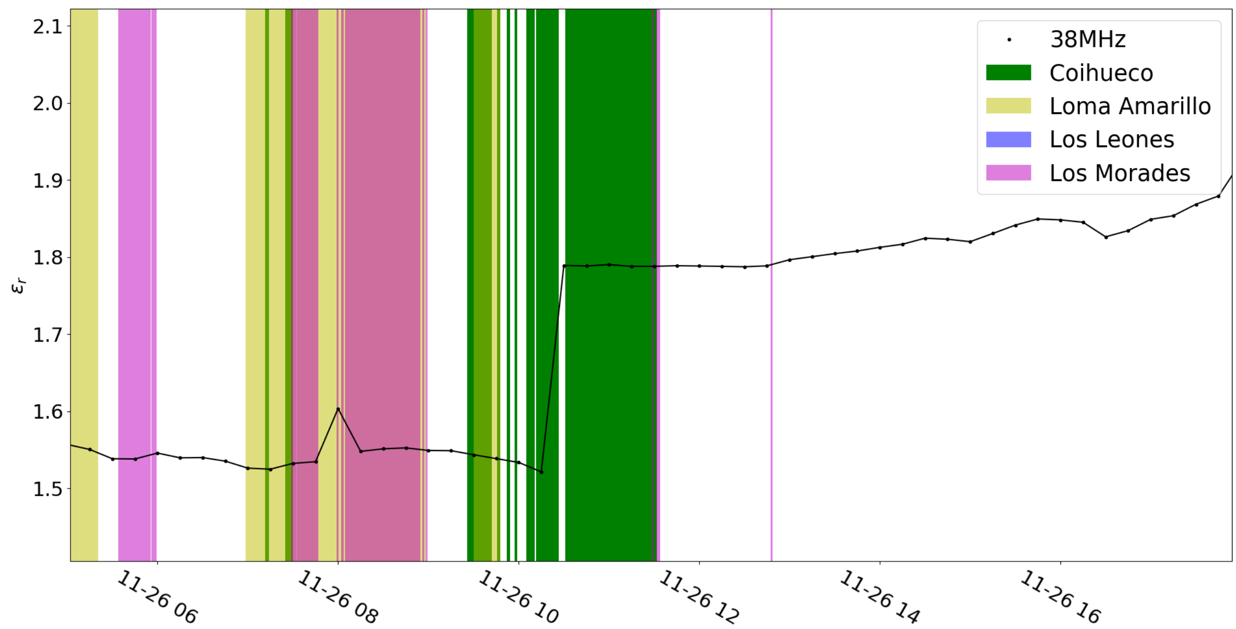

(a) A clear rise in permittivity can be seen for November 2015, the nearest FD in Coihueco also registered rain.

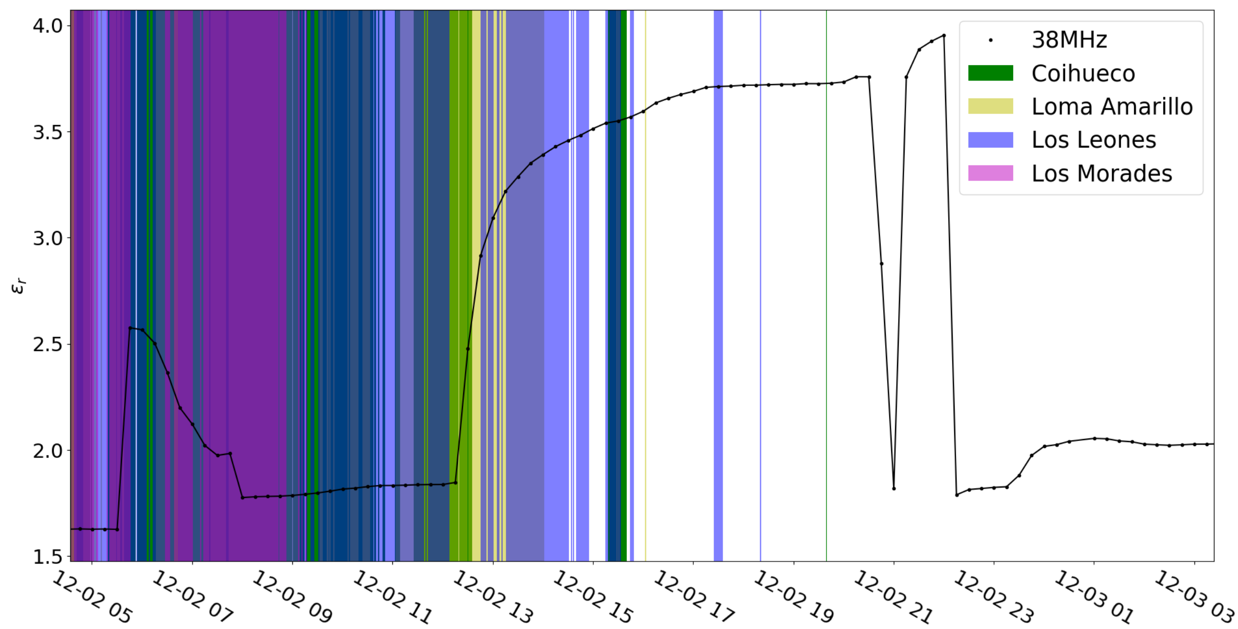

(b) The permittivity peaks again in December 2016, all FD stations recorded precipitation.

Figure 32: Peaks of the permittivity correlated to rain at the FD buildings.

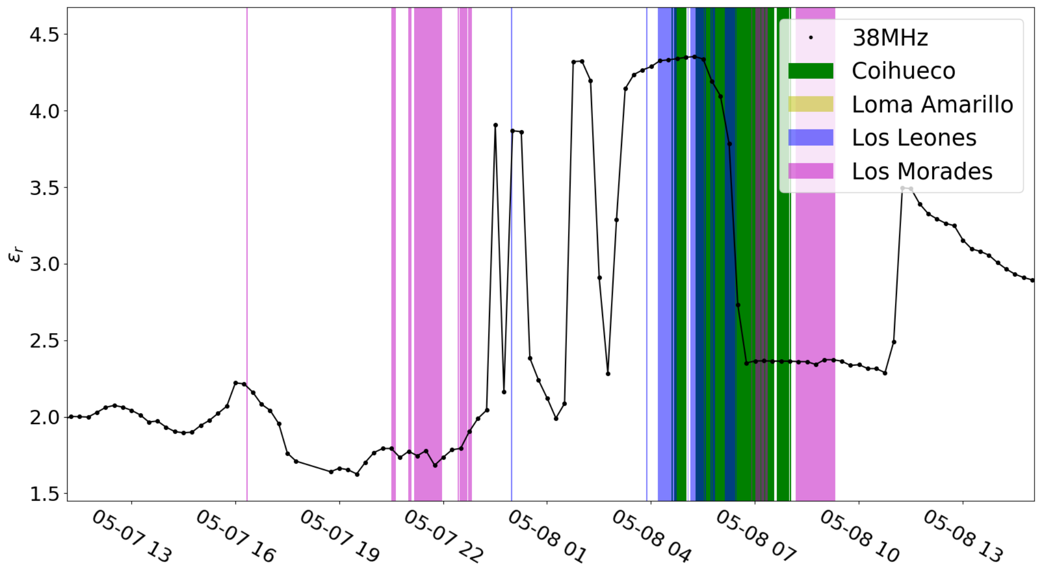

Figure 33: The plots shows an increase of 180 %, the largest rise in the data set.

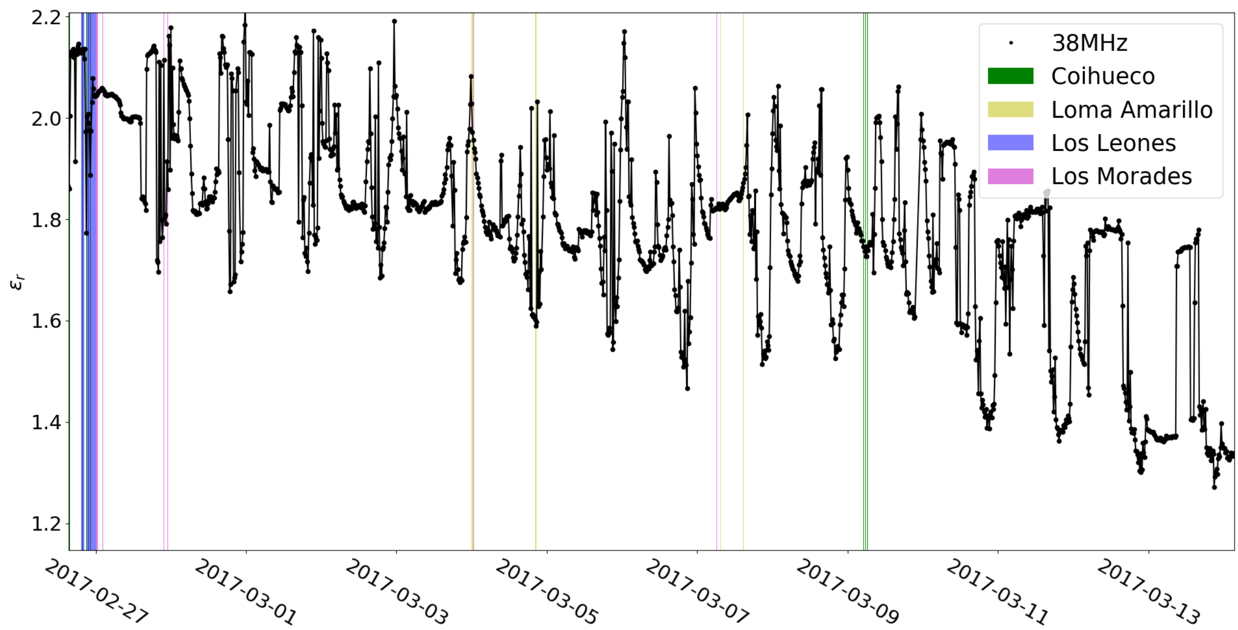

Figure 34: A decrease of the permittivity is visible caused due to missing rain.

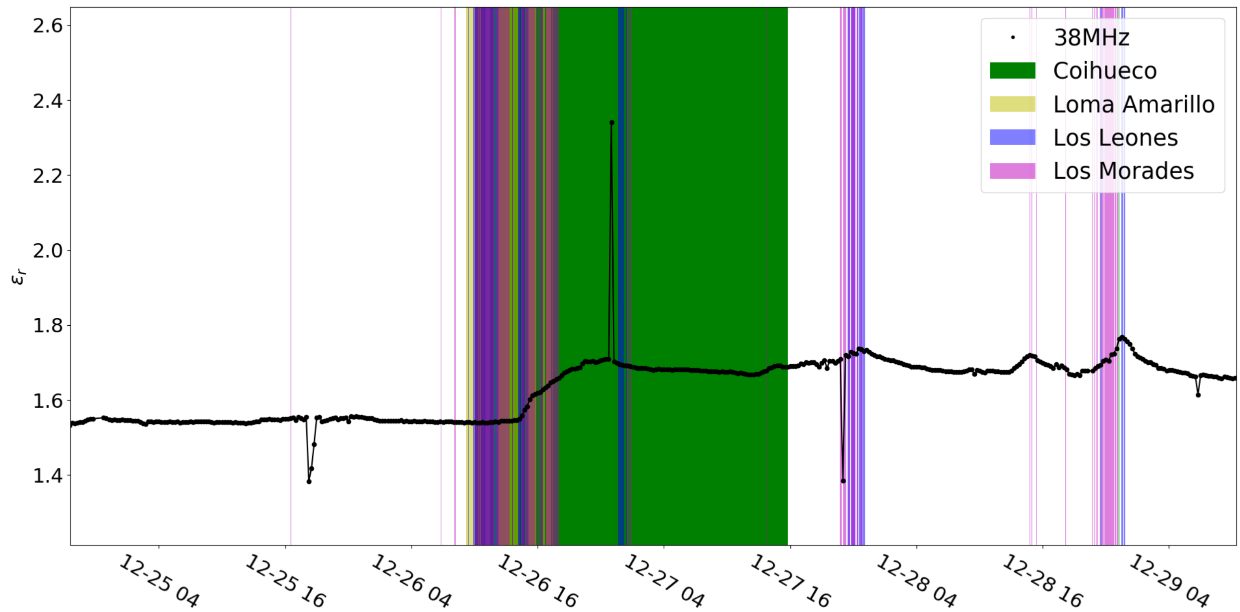

(a) Even tough it rains for a long time at Coihueco in December 2016, only a slight increase is visible.

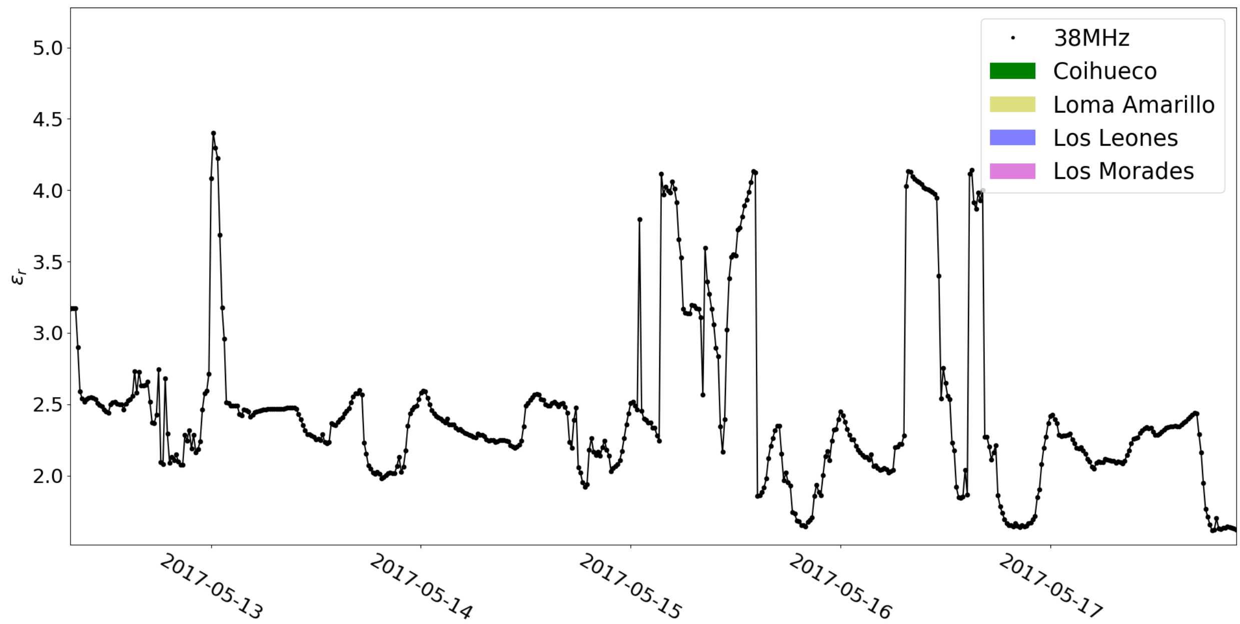

(b) Peaks are visible, that cannot be explained by variation in the air humidity; rain is also not visible.

Figure 35: The plots show bad examples for the qualitative correlation of the FD weather data and permittivity.

The first plot (Fig. 35a) demonstrates the importance of the amount of rain. In this case, all FDs measured rain, but, except for one datapoint, only a small rise in the permittivity is visible. A relative difference of about 15 % is observed and is most likely to be caused by rainfall. Just by the time and number of triggered FDs one would expect this rise to be larger. The second example (Fig. 35b) is about the location of the acquired data. Peaks appear, which are similar to those already seen on rainy days. But here, the rain is missing, no FD station was triggered. As the height of the values can only be explained by rain, the precipitation developed above the setup or passed the setup, but without hitting the FDs.

Nevertheless, a clear influence of the rain can be seen. Most of the peaks that appear can be correlated qualitatively with the precipitation. This could be tuned further, for example by taking the windspeed and winddirection into account. But due to the large distances, the uncertainty would get out of hand and this is unpractical for qualitative statements. In fact, the lack of rain data should be fixed and a new, complete analysis and quantitative relations should be produced.
Despite that no clear conclusion about the correlation of rain and permittivity can be found, relative increases of up to 180 % can be seen. The question now is, wether this deviation is causing a measurable change on the measured radio signals. This will be discussed in the following chapter.

6 Effects on the galactic noise

The sensitivity to the galactic noise was a design goal of the AERA setup. It is used for the calibration of the antenna stations. The noise level is measured at different frequencies. One of them is 38MHz, which is also used in this thesis for the permittivity. This is easier to look at compared to signals from actual air showers, when investigating the permittivity. One advantage is the amount of data. The noise is omnipresent and is measured every 100 seconds at AERA. Signals caused by particle showers are less frequent. The second advantage is the comparably low statistical fluctuation of the noise.
The noise is measured by all radio stations, for this analysis channel one of station 126 is used as this station is the closest one to AERAWS. The amplitude of the noise is measured in ADC counts, so, the absolute value is not calculated here since only the variation is important.
The correlation of the two quantities is depicted in Fig. 36. Two types of investigation are shown, the first one (Fig. 36a and 36b) takes the mean of the three temporally nearest measurements of the noise into account for every measured permittivity. The second investigation (Fig. 36c and 36d) shows the correlation of the maximal value of the permittivity and the mean noise for each day.

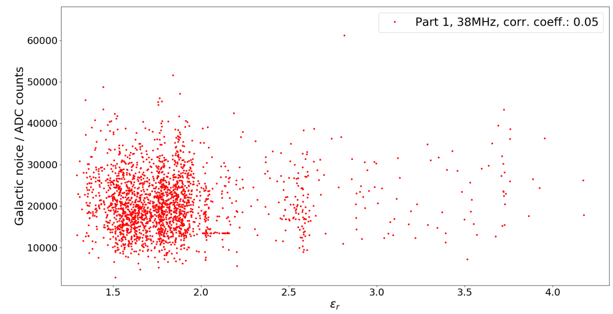

(a)

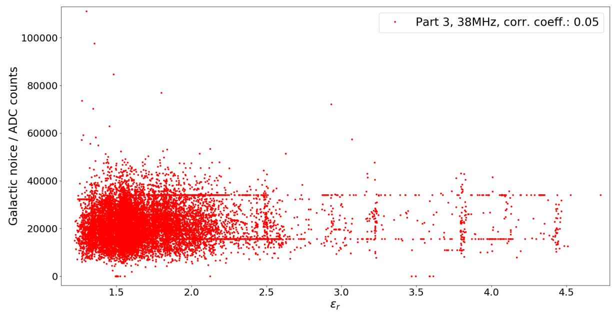

(b)

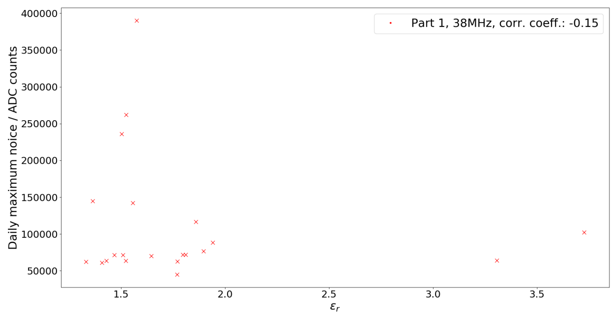

(c)

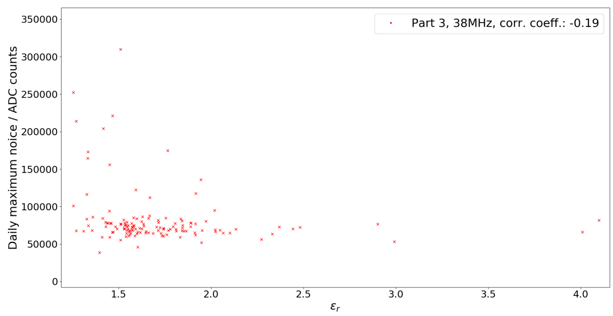

(d)

Figure 36: The correlation of the permittivity with the galactic noise is shown; the top row describes the correlation for each value, the bottom row shows the correlation with the maximal value for the day.

No indication of a correlation can be found. This means that the effects of the variation in the permittivity is low and in especially smaller than the statistical fluctuation. This

agrees with the assumption that the permittivity can be approximated as a constant. To clearly confirm this point, one has to control or unfold other effects that influence the noise so that the sesitivity to the effect on the permittivity is increased.
It has to be clarified, that only because the effect of the permittivity cannot be detected on the small signals of the galactic noise compared to statistical fluctuations, it does not conclude that there is no significant effect on the much larger signals of cosmic rays. Here it is concluded only that with the galactic noise no effect of the permittivity is detectable.

7 Summary and outlook

In this thesis, the data of permittivity measurement [4] at the Pierre Auger Observatory was investigated as systematic effect for the radio detection of cosmic rays. The functionallity of the setup is limited in quantity as well as in quality. Since the beginning of the measurement, it worked less than half of the time due to crashes of the controlling or power supply defects. This did not only reduce the quantity of measurements, but also the quality by malfunctioning while measurements. Part of the data had to be rejected alltogether. To qualify the data a model has been succesfully developed to describe the frequency dependence of the permittivity. Another significant challenge is the missing calibration of the secondary VNA. Irregularities can be seen, most likely caused by this. This cannot be solved without further study of the setup, which is not accessible while this study.

When compared to literature and comparable measurements, the absolute values of the measured permittivity was found to deviate. The average permittivity is $\varepsilon_\mathrm{r} = 1.83 \pm 0.40$ for part I and $\varepsilon_\mathrm{r} = 1.73 \pm 0.43$ for part III compared to a value expected in the range of 5 - 8 [2]. This analysis focused therefore on the time developement that shows a steady behaviour and the relative values are considered reliable. A sophisticated analysis of the correlation with enviromental effects is difficult due to different challenges. The lack of precipitation data was not expected, and also large distances or low quality of enviromental data are reasons for difficulties. Nonetheless, correlations with the air humidity and temperature were seen qualitatively. Daily variations caused by this were determined to about 4 %, larger effects are shown for rainfall. Through bool values, peaks of the permittivity were connected to rain and features of the developement were explained. Relative changes caused by rain of 180 % are detected. The analysis also shows other examples for this method to fail and justifies the urge for reliable data about preciption.

The permittivity has no visible effects on the measurement of the galactic noise, the correlation coefficients are small and below 0.2 absolutely. The statistical fluctuation might be too large, so the rather weak influence of the permittivity can not be seen.

One has to ask in the end, what can be done to improve the results and what can be achieved through that? The first part of the question is easy to answer. The different weather stations just need to be repaired. The permittivity measurement has to be recallibrated and the setup should be moved to the central radio station. Through different power banks, the supply would be guaranteed. Another advantage is the location, the CRS is more central in AERA and the results would be more universal for the array. If the locations of the permittivity measurement is not moved, the AERAWS has to be repaired to measure all quantities. Independently, the rain sensor of the CRS needs to exchanged.

The secondary question can be fully answered only in detail and extensively. Here, just a quick overview is given what was planned in advance of this thesis, but could not be done through the lack of reliable data. One big point is to make more quantitative state-

ments about the time and weather dependence. The time dependence and especially the variation for different seasons could not be done, as not all months are equally or at all represented by the data. For this type of correlation, there should be at least 3 years fully measured data, so that the statistical fluctuations are visible and can be estimated. This is only related to the weather dependence. The correlation with temperature and humidity were slightly local visible, the correlation with the preciption could not be calculated.
The galactic background does not show any varying caused by the permittivity. Either the correlation is too small to see effects or the fluctuation in the background dominates the spectrum.
Another aspect would be a further analysis of the influence on the radio signals by the permittivity. A possible investigation is to look for similar SD signals (same energy, arrival direction, location e.g.). If the permittivity has different values, the recieved radio signals should look different in amplitude or time resolution. These kind of analysis would bring up new awareness, whether the chosen constant value is a acceptable approximation.

References

[1] The Pierre Auger Collaboration, 'The Pierre Auger Observatory Upgrade - Preliminary Design Report', arXiv:1604.03637

[2] R. Krause, 'Antenna Development and Calibration for Measurements of Radio Emission from Extensive Air Showers at the Pierre Auger Observatory', PhD thesis (RWTH Aachen University, 2018)

[3] Informations about the permittivity I, `https://de.wikipedia.org/wiki/Permittivit%C3%A4t` (19.08.2018)

[4] M. Kasten, 'Aufbau einer Mess-Station zur kontinuierlichen Bestimmung der Bodeneigenschaften beim Auger Engineering Radio Array', Diploma thesis (University of Wuppertal, 2015)

[5] V. Hess, Physik. Zeitschrift XIII, 1084-1091 (1912)

[6] J. Rautenberg, University lecture 'Grundlagen der Elementar- und Astroteilchenphysik' (2017)

[7] W. Heitler, The Quantum Theory of Radiation, third ed., Oxford University Press, London, 1954

[8] The Pierre Auger Collaboration, 'The Pierre Auger Observatory: Contributions to the 35th International Cosmic Ray Conference (ICRC 2017)', arXiv:1708.06592

[9] K. Weidenhaupt, 'Antenna Calibration and Energy Measurement of Ultra-High Energy Cos- mic Rays with the Auger Engineering Radio Array', PhD thesis (RWTH Aachen University, 2014)

[10] Fresnel equations, `https://en.wikipedia.org/wiki/Fresnel_equations` (21.10.2018)

[11] Informations about the permittivity II, `https://www.eoas.ubc.ca/courses/eosc350/content/methods/gpr-06.htm` (20.10.2018)

[12] Reference values for different mediums, `http://www.kayelaby.npl.co.uk/general_physics/2_6/2_6_5.html` (20.10.2018)

[13] Specifications of the VNA, `http://miniradiosolutions.com/minivna-pro/` (27.08.2018)

[14] Software of the VNA, `http://vnaj.dl2sba.com/` (27.08.2018)

[15] J. Rautenberg, private communication

[16] R. Krause, private communication

[17] Manual for the rain sensor, https://www.vaisala.com/sites/default/files/documents/M210906EN-C.pdf (24.10.2018)

[18] Weather data from Malargüe airport, http://rp5.am/Weather_archive_in_Malargue_(airport) (21.09.2018)

[19] Satellite picture of the observatory, https://www.scribblemaps.com/ (11.10.2018)